DESIGN OF ACTIVE LOCALIZATION SYSTEM FRONT-END BUILDING BLOCKS FOR MR-GUIDED INTERVENTIONAL PROCEDURES

by

İsmail Gerçek

B.S. , Electronics and Communication Engineering, İ.T.Ü. , 2006

Submitted to the Institute for Graduate Studies in
Science and Engineering in partial fulfillment of
the requirements for the degree of
Master of Science

Graduate Program in Electrical & Electronics Engineering
Boğaziçi University

2009

DESIGN OF ACTIVE LOCALIZATION SYSTEM FRONT-END BUILDING BLOCKS FOR MR-GUIDED INTERVENTIONAL PROCEDURES

APPROVED BY:

Prof. Günhan Dündar (Thesis Supervisor)	.....
Asst. Prof. Arda Deniz Yalçınkaya	.....
Assoc. Prof. Dr. Cengizhan Öztürk	.....

DATE OF APPROVAL: 16.September.2009

ACKNOWLEDGEMENTS

I would like to thank my advisor, Prof. Günhan Dündar, for his encouragement, interest, and patience. Personally, I would like to thank him for sharing his knowledge which has enriched my study in electronics. I also would like to thank to Asst. Prof. Arda Deniz Yalçınkaya and Asst. Prof. Şenol Mutlu for their valuable advice and help. I'm grateful to Assoc. Prof. Dr. Cengizhan Öztürk and Murat Tümer for fruitful discussions which gave an insight on MR.

This thesis would not have been possible without Dağhan Gökdel and Baykal Sarıoğlu, I would like to thank them for their encouragement and help in lab work. I would like to show my gratitude to Orhan Mert and Ozan Aktan for their valuable discussions and support.

Lastly, I offer my regards and blessings to all of those who supported me in any respect during the completion of the project.

ABSTRACT

DESIGN OF ACTIVE LOCALIZATION SYSTEM FRONT-END BUILDING BLOCKS FOR MR-GUIDED INTERVENTIONAL PROCEDURES

In interventional procedures imaging plays an important role, as quick and accurate determination of the interventional device position and tissue structures are crucial for the procedure. Usually interventional procedures are being conducted in X-ray fluoroscopy. However, it is highly desirable to use the MRI technology for interventional procedures, since MRI is a safe and reliable medical imaging method providing good soft tissue contrast while avoiding harmful ionizing radiation. New interventional instruments has to be designed for this purpose since there are certain constraints regarding imaging and localization process and MR physics.

One such constraint is heating of conductors. MRI systems transmit received MRI signals through electrical cables. This design is effective for the conventional case, where receive coils are placed outside of the subject body. However, for the internal coils safety improvements has to be made, mainly due to the heating problem of conducting material under strong RF waves transmitted by the MRI system. To overcome the heating problem optical transmission of data and power is used.

In this thesis an active localization system for catheters, which is intended to be used in interventional procedures in MRI , is studied. The purpose of the study is to design some main building blocks for such an active localization system front-end. A dickson charge pump operating with alternating input signal at 100MHz with an amplitude of 1V and generating 1.94V at its output for 100K ohm load resistance

is designed. Different receive coil sizes are studied and obtained results show Q^2xR values of 1300 can be reached with the processing technology at hand. The gain stage is designed as a Low Noise Amplifier, for 64MHz and 123MHz precession frequencies. $4.112dB$ noise figure is obtained for LNA@64MHz and $4.813dB$ for LNA@123MHz.

ÖZET

GİRİŞİMSEL MRG İÇİN AKTİF KATETER KONUM BELİRLEME SİSTEMİ GİRİŞ KATI YAPI BLOKLARININ TASARIMI

Girişimsel cihazların konumunu ve doku yapısını hızlı ve yüksek hassasiyetle belirlemek için girişimsel cerrahide görüntüleme önemli bir rol oynar. Girişimsel işlemler genellikle x-ışını teknolojisi kullanılarak uygulanmaktadır. Ancak MR ile görüntüleme imkanları gerek yüksek doku kontrastı sağladıkları gerekse de zararlı x-ışınlarıyla calışmadıkları için daha uygun bulunmaktadır. Bu cerrahi işlemler için MR görüntüleme sistemlerinin gerektirdiği bazı kısıtlamalara uygun cihazların tasarımı gereklidir.

Bu kısıtlardan bir tanesi iletken cisimlerin cihazın içinde, dokulara zarar verecek kadar ısınabilmesidir. Alıcı antenin vücut dışında bulunduğu normal MR görüntüleme uygulamalarında bir sorun oluşmasa da girişimsel MRG'de hasta güvenliği için tehdit oluşmaktadır. Bu kısıt göz önünde bulundurularak tasarımda optik veri ve güç akışı sağlanmıştır.

Bu tez süresince girişimsel MRG için aktif kateter konum belirleme sistemi üzerine çalışılmıştır. Çalışma kapsamında giriş katı temel yapı bloklarından olan güç katı, alıcı anten ve düşük gürültülü kuvvenlendirici tasarımları gerçekleştirilmiştir. Dickson mimarisinde tasarlanan gerilim çarpıcı girişinde 1V genlikli 100MHz frekansında salınım yapan giriş işaretine karşılık 100K ohm yük direncinde 1.94V genliğinde gerilim üretebilmektedir. Farklı boyutlarda tasarımı yapılan alıcı antenlerinin Q^2xR değerleri $1300ohm$'a kadar çıkmaktadır. İki farklı çalışma frekansında tasarlanan düşük gürültülü kuvvetlendirici katları giriş işaretine 64MHz için $4.112dB$, 123MHz için ise

$4.813dB$ gürültü eklemektedir.

TABLE OF CONTENTS

ACKNOWLEDGEMENTS iii
ABSTRACT iv
ÖZET vi
LIST OF FIGURES x
LIST OF TABLES xiv
LIST OF SYMBOLS/ABBREVIATIONS xv
1. Introduction 1
1.1. A Short History of MRI 1
1.2. Magnetic Resonance 2
1.2.1. Physical Background 2
1.2.1.1. Nuclear Magnetism 2
1.2.1.2. Resonance and Relaxation 6
1.2.2. Generating an Image 7
1.2.2.1. Imaging parameters 7
1.2.2.2. Back projection 10
1.2.2.3. 2D Fourier Transform 11
1.3. Outline 11
2. Power Generation 13
2.1. Charge Pump 14
2.1.1. Introduction 14
2.1.2. Theory 14
2.1.2.1. Cockcroft-Walton Charge Pump 14
2.1.2.2. Dickson Charge Pump 16
2.1.3. Design Considerations 16
2.2. Design 17
2.2.1. Charge Pump 17

2.3. Results 18
3. Receive Antenna 21
3.1. Design and Simulation 21
3.1.1. Geometrical model 21
3.1.2. Matching 24
3.1.3. Resonant Coil 27
3.2. Fabrication and Measurements 33
4. Low Noise Amplifier 37
4.1. Introduction 37
4.2. Theory 38
4.2.1. Noise 38
4.2.1.1. Thermal Noise 38
4.2.1.2. Shot Noise 39
4.2.1.3. Flicker Noise 39
4.2.2. Noise Sources in FETs 41
4.2.3. Noise Analysis in FETs 43
4.2.4. Linearity 45
4.2.5. Matching 49
4.2.6. Stability 50
4.2.7. Common LNA Architectures 50
4.3. Design and Simulation 53
4.3.1. Design @63.5MHz 54
4.3.2. Design @123MHz 54
5. Conclusion and Future Work 62
REFERENCES 63

LIST OF FIGURES

Figure 1.1. Precession of a spinning proton 4

Figure 1.2. Alignment of nuclei and net magnetization vector 4

Figure 1.3. Energy levels of the nuclei under a magnetic field 5

Figure 1.4. Net magnetization vector when applied an RF energy 7

Figure 1.5. Free Induction Decay 8

Figure 1.6. NMR spectrum of Ethanol (CH_3CH_2OH) with Carbon-13 Spectroscopy 10

Figure 1.7. Spatial encoding and back projection 11

Figure 2.1. Operation of voltage doubler 15

Figure 2.2. Cockcroft-Walton Charge Pump 15

Figure 2.3. Dickson Charge Pump 16

Figure 2.4. Charge pump schematic for a single stage 18

Figure 2.5. Power conversion circuit 19

Figure 2.6. Output potentials under different load resistances 20

Figure 3.1. 3-D view for $1mm$ x $1mm$ coil with 1.5 turn 22

Figure 3.2. 3-D view for $1.5mm$ x $1.5mm$ coil with 2.5 turn 23

Figure 3.3. 3-D view for $2mm$ x $2mm$ coil with 4.5 turn 23

Figure 3.4. 3-D view for $3mm$ x $3mm$ coil with 4.5 turn 24

Figure 3.5. Schematic for ADS AC Analysis 25

Figure 3.6. AC analysis results for $1mm$ x $1mm$ coil 25

Figure 3.7. AC analysis results for $1.5mm$ x $1.5mm$ coil 26

Figure 3.8. AC analysis results for $2mm$ x $2mm$ coil 26

Figure 3.9. AC analysis results for $3mm$ x $3mm$ coil 28

Figure 3.10. Schematic for ADS S-Parameter Analysis 28

Figure 3.11. Simulated S_{11} for $1mm$ x $1mm$ coil 29

Figure 3.12. Simulated S_{11} for $1.5mm$ x $1.5mm$ coil 29

Figure 3.13. Simulated S_{11} for $2mm$ x $2mm$ coil 30

Figure 3.14. Simulated S_{11} for $3mm$ x $3mm$ coil 30

Figure 3.15. Layout for coils 33

Figure 3.16. Measured S_{11} for $1mm$ x $1mm$ coil 34

Figure 3.17. Measured S_{11} for $3mm$ x $3mm$ coil 35

Figure 3.18. Measured S_{11} on smith chart for $1mm$ x $1mm$ coil 35

Figure 3.19. Measured S_{11} on smith chart for $3mm$ x $3mm$ coil 36

Figure 4.1. Noise sources in MOSFETs 43

Figure 4.2. Two-port model for noise analysis in MOSFETs 44

Figure 4.3. Graphical representation of 1-dB compression point 47

Figure 4.4. Signal spectrum of a nonlinear block 48

Figure 4.5. Graphical interpretation of IIP3 49

Figure 4.6. Common LNA architectures 51

Figure 4.7. Schematic of the LNA@63.5MHz 55

Figure 4.8. Simulated noise figure of the LNA@63.5MHz 56

Figure 4.9. Simulated S-parameters of the LNA@63.5MHz 56

Figure 4.10. Simulated stability factor of the LNA@63.5MHz 57

Figure 4.11. Simulated harmonic balance of the LNA@63.5MHz 57

Figure 4.12. Schematic of the LNA@123MHz 58

Figure 4.13. Simulated noise figure of the LNA@123MHz 59

Figure 4.14. Simulated S-parameters of the LNA@123MHz 60

Figure 4.15. Simulated stability factor of the LNA@123MHz 60

Figure 4.16. Simulated harmonic balance of the LNA@123MHz 61

LIST OF TABLES

Table 1.1. Nuclei of Medical Interest and Gyromagnetic Ratios 5

Table 3.1. Simulated impedance and quality factor values 27

Table 3.2. Simulated component values for the matching network 27

Table 3.3. Simulated Q^2xR values for $3mmx3mm$ coil with 4.5 turns, $60um$ line width 31

Table 3.4. Simulated Q^2xR values for $3mmx3mm$ coil with 4.5 turns, $30um$ line width 31

Table 3.5. Simulated Q^2xR values for $3mmx3mm$ coil with 4.5 turns 31

Table 3.6. Simulated Q^2xR values for $3mmx3mm$ coil with 4.5 turns, $90um$ line spacing 32

Table 3.7. Simulated Q^2xR values for higher turn numbers 32

Table 3.8. Measured impedance and S_{11} values 34

LIST OF SYMBOLS/ABBREVIATIONS

C_{ox}	Gate oxide capacitance
F	Noise factor
h	Planck's constant
$\vec{J}$	Angular momentum
k	Boltzmann's constant
K	Stern stability factor
°K	Degrees in Kelvin
L	Gate length
Q	Quality factor
$R_{\diamond}$	Sheet resistance
T1	Longitudinal relaxation time
T2	Transverse relaxation time
W	Gate width
δ	Gate noise coefficient
γ	Gyromagnetic ratio in $[T/MHz]$
$\vec{\Gamma}$	Torque
ω	Angular frequency
AC	Alternating current
ADS	Advanced Design System
DR	Dynamic range
EPI	Echo planar imaging
FET	Field effect transistor
FID	Free induction decay
fMRI	Functional magnetic resonance imaging

IP3	Third order intercept point
IIP3	Third order input intercept point
IMP	Intermodulation products
LNA	Low noise amplifier
MOS	Metal oxide semiconductor
MOSFET	metal oxide semiconductor field effect transistor
MR	Magnetic resonance
MRA	Magnetic resonance angiography
MRI	Magnetic resonant imaging
NF	Noise figure
NMR	Nuclear magnetic resonance
P_{1db}	1-db compression point
RF	Radio frequency
RFID	Radio frequency identification
SNR	Signal to noise ratio
TE	Time to echo
TI	Inversion delay time
TR	Repetition time

1. Introduction

Magnetic Resonance Imaging (*MRI*) is a state of the art technology allowing us to make cross sectional images of the body tissues and today is widely used in medical procedures. In contrast to medical radiography, another widely used medical imaging technology, MR systems don't use ionizing radiation which is harmful for the living tissue. In addition, images with higher contrast values can be achieved non-invasively, especially for the soft tissue. These advantages led to further development and in time MRI systems have evolved from just being a tomographic imaging technique to a volume imaging technique. Moreover, different applications have been developed such as Magnetic Resonance Angiography (*MRA*) and Functional MRI (*fMRI*). *MRA* is used to makes images of the blood vessels, whereas *fMRI* is mainly used in neuroscience to study which regions of the brain are responsible for thought and motor control. Today, MR technology is used in many clinical applications and replacing ionizing imaging techniques. One such application is the use of MR imaging technology for interventional medical procedures. In this thesis, an active localization system for catheters to be used in such a medical procedure is studied and some building blocks are designed.

1.1. A Short History of MRI

First commercial MRI Systems used in clinical applications came to life in 1980s. But, the start of this success story goes many decades back in time. Joseph Larmor stated the relation, known as the *Larmor Equation*, between angular frequency of precession of nuclear spins and the strength of the magnetic field they are exposed to. Isidor Isaac Rabi and his group of researchers discovered that in a two-state system, changing the states of the nuclei is possible by introducing a quantum level of energy. Isaac Rabi received a Nobel prize in Physics for describing how magnetic fields and nuclei were associated. He also coined the term *nuclear magnetic resonance*. After these

fundamental findings two scientist, Felix Bloch and Edward Purcell, independently explained the magnetic resonance phenomenon in 1946 and both were awarded the Nobel Prize six years later in 1952.

At first, nuclear magnetic resonance was used mainly by chemists and physicist to analyze chemical compounds. The applications of nuclear magnetic resonance widened after Raymond Damadian's discovery in 1971. He showed that the relaxation times of normal tissues and tumors differed; which, opened up the possibilities of using NMR for diagnostic procedures in clinic. The first practical demonstration was made by Paul Lauterbur in 1973. Paul Richard Ernst suggested to use phase and frequency encoding for imaging purposes in 1975. In 1976, Raymond Damadian was able to generate an image of the chest cavity of a live man. In 1980s, NMR was commercialized and used in clinical applications. With the use of Echo-Planar Imaging (*EPI*) a real-time movie of a heart cycle was constructed in 1987. Magnetic Resonance Angiography (*MRA*) was used in 1987 by Charles Dumoulin. In 1993 Functional MRI (*fMRI*) was developed and opened new opportunities for neuroscientists to examine the brain.

Today, NMR and MRI has many uses in physics, chemistry and medicine. The speed and precision of the equipment is still in development and open to many advances in the future.

1.2. Magnetic Resonance

1.2.1. Physical Background

1.2.1.1. Nuclear Magnetism. Neutrons and protons, which are the subatomic particles composing the nuclei, have the quantum property of spin. The spin quantum number S determines the overall spin of the nucleus. Even number of neutrons or even number of protons make pairs so their overall spin is zero(e.g. if there are two protons in the

nucleus, one proton has a spin of 1/2 while the other proton has a spin of -1/2, which add up together to be zero).

A nucleus with a spin different than zero presents a magnetic moment. When such nuclei is placed in a magnetic field with strength B a torque is applied on the magnetic moment:

$$\vec{\Gamma} = \vec{\mu} \times \vec{B} = \gamma \vec{J} \times \vec{B} \tag{1.1}$$

where $\vec{\Gamma}$ is the torque, $\vec{J}$ is the angular momentum vector, $\vec{B}$ is the external magnetic field, and equation constant γ is called *gyromagnetic ratio* of the nucleus. The nucleus shows a motion as a result of this torque applied, along with its spin it starts to precess about the axis of the applied magnetic field. The precession frequency is called the *Larmor* frequency after *Joseph Larmor* and the relation is stated with the *Larmor* equation:

$$\omega = \gamma \times B \tag{1.2}$$

where equation constant γ is the gyromagnetic ratio of the nucleus and ω is the frequency of precession (Figure 1.1). In classical mechanics terms, this phenomenon is similar to a gyroscope's motion on Earth, where gyroscope's angular momentum interacts with the Earth's. Gyromagnetic ratios for some nuclei of medical interest are presented in Table 1.1. In medical imaging, hydrogen is of highest interest because of its concentration in the body and high gyromagnetic ratio.

In a mass (the body for medical imaging) magnetic dipole moment vectors of nuclei with spin are randomly distributed and the mass itself doesn't have any magnetic moment(Figure 1.2). When they are put in a magnetic field other than precession they are aligned about the axis of the applied magnetic field(Figure 1.2). Nuclei under

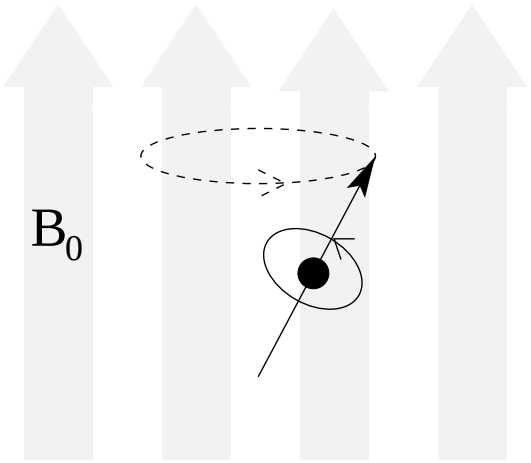

Figure 1.1. Precession of a spinning proton

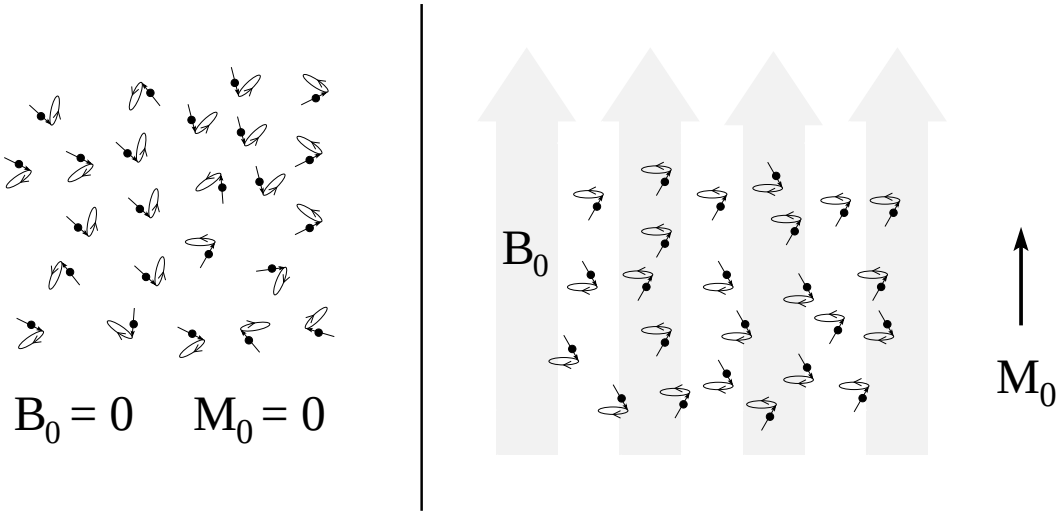

Figure 1.2. Alignment of nuclei and net magnetization vector

Table 1.1. Nuclei of Medical Interest and Gyromagnetic Ratios

Nuclei	Unpaired Protons	Unpaired Neutrons	Net Spin	Gyromagnetic Ratio (MHz/T)
^{1}H	1	0	1/2	42.58
^{2}H	1	1	1	6.54
^{31}P	1	0	1/2	17.25
^{23}Na	1	2	3/2	11.27
^{14}N	1	1	1	3.08
^{13}C	0	1	1/2	10.71
^{19}F	1	0	1/2	40.08

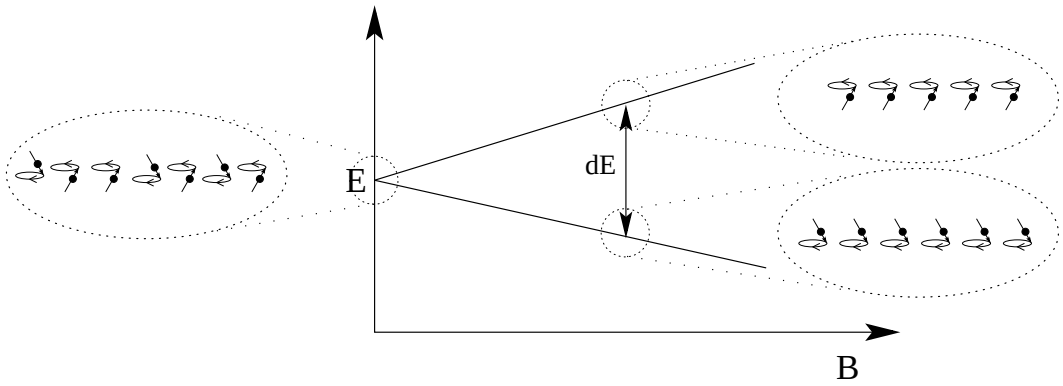

Figure 1.3. Energy levels of the nuclei under a magnetic field

the magnetic field are said to be polarized and a net magnetization is formed. It is important to note that not every single nucleus is polarized in that way, it is just one in a million nuclei according to *Boltzmann* statistics. At room temperature the number of nuclei in the higher energy state N^- is slightly less than the number of nuclei in the lower energy state N^+. The relation is as follows according to Boltzmann statistics:

$$N^-/N^+ = e^{-E/kT} \tag{1.3}$$

where E is the difference in energy levels, k is the Boltzmann constant and T is the temperature in °K.

Among medically interesting material, the nucleus of ^{1}H has two possible spin states, it is either s=1/2 or s=-1/2, these states are also referred as spin-up or spin-down. The energy that a magnetic moment μ has, when placed in a magnetic field B, is given by:

$$E = -\mu B \tag{1.4}$$

where B is chosen to be along the z axis. The equation states that different nuclear spin states having different energy levels in a magnetic field(Figure 1.3). In classical mechanics terms, if we think the nuclei as being small magnets; that is to say, some nuclei are aligned with the magnetic field, being in the lower energy state and the others are not, being in the higher energy state. As can be deduced from Boltzmann statistics the number of nuclei in the lower energy state increases proportionally with the energy difference that spin states experience under a certain magnetic field. Difference in the energy levels increases with the increasing magnetic field. At this point we can deduce that higher magnetic fields yield a higher net magnetization of the mass under examination, hence results in better sensitivity in imaging applications.

1.2.1.2. Resonance and Relaxation. The Larmor frequency is also referred as the resonance frequency of the nuclei in magnetic field. That is because a single nucleus can change its spin state with absorbing a photon which has an energy equal to the energy difference between the two states. The energy of the photon is given by:

$$E = hV \tag{1.5}$$

where V is the frequency of the photon, and h is the Planck's constant. Here the resonance frequency has to be equal to the Larmor frequency, at which the nucleus is precessing, for a state change. In medical applications this excitation frequency is in the RF range of the electromagnetic spectrum for hydrogen nuclei.

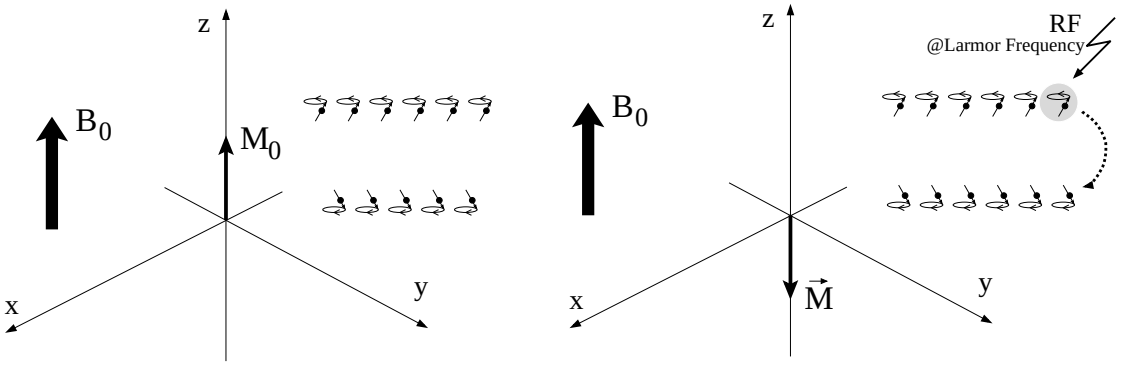

Figure 1.4. Net magnetization vector when applied an RF energy

By transmitting an electromagnetic wave at the resonance frequency total number of nuclei in the higher energy state can be increased. In the absence of this electromagnetic wave, a slightly higher number of nuclei were aligned with the magnetic field, hence the net magnetization vector was directed to the z axis(assuming the magnetic field vector also lies in the z axis). With the presence of electromagnetic wave the direction of the net magnetization vector changes from the z direction to the $-z$ direction (Figure 1.4). After the RF excitation, nuclei return to their initial condition emitting electromagnetic waves at Larmor frequency. The signal generated by the nuclei has information about the nuclei under examination and called *Free Induction Decay* (*FID*)(Figure 1.5). This process of returning to the initial phase is called the *relaxation*. Some information can be extracted out of the RF wave emitted from the nuclei, that is how NMR and MRI works in principle. There are some different methods applied for generating images, the next section summarizes some concepts for generating images.

1.2.2. Generating an Image

1.2.2.1. Imaging parameters. In MRI systems it is vital to understand three parameters, namely *Spin Density*, *T1 relaxation time* and *T2 relaxation time*. Moreover when applying an electromagnetic wave(called RF pulse sequence) for excitation there are certain timings that affect the produced image. Most used ones can be listed as *Repetition Time (TR)*, *Inversion-Delay Time (TI)* and *Time-to-Echo (TE)*.

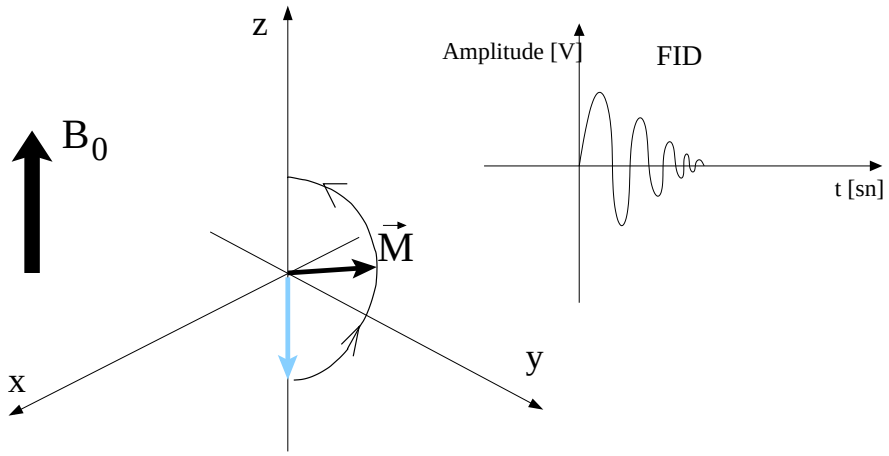

Figure 1.5. Free Induction Decay

As explained before, the extra number of nuclei in low-energy level creates a net magnetization vector(M_0) along the static magnetic field (B_0). Since emitted RF signal, which is the FID, is proportional to M_0, a dense part of the material will produce a more powerful RF signal. *Spin Density* is a term used to refer to the concentration of hydrogen nuclei available to produce the RF signal. In human body, different tissues have different spin densities, so they can be differed in an MR image. Such images are referred as *Spin Density Weighted* images.

The net magnetization vector M_0 lies on the z axis, and there are no transversal components such as M_x and M_y. If we give the right amount of energy to the system, the net magnetization vector can be placed on the XY-plane. Such a pulse is called a 90° pulse since it can rotate M_0 by 90°s. After the excitation the system relaxes and once again $M_z = M_0$. $T1$ is the time constant of this relaxation:

$$M_z = M_0(1 - e^{-t/T1}) \tag{1.6}$$

$T1$ is also referred as *Longitudinal Relaxation Time* or *Spin-Lattice Relaxation Time*.

M_x and M_y components of the net magnetization vector are formed after a 90° pulse, say at time zero $M_y = M_0$. Since the nuclei is under a magnetic field they

experience a precession at the Larmor frequency this time on the XY-plane with the effect of the 90° RF pulse given to the system. As a result of the molecular interactions and differences every single nucleus doesn't experience the same magnetic field. This results in dephasing of magnetic moment vectors of the nuclei, some nuclei precess slightly faster whereas some precess slower. Magnitude of the transversal component of the net magnetization vector starts to decay. $T2$ is the time constant of this relaxation:

$$M_{xy} = M_{xy0}(1 - e^{-t/T2}) \tag{1.7}$$

$T2$ is also referred as *Transverse Relaxation Time* or *Spin-Spin Relaxation Time*. When this process is observed it is seen that M_{xy} decays faster than expected. The reason is the inhomogeneity in magnetic field and RF pulses. The latter process is the one experienced in practice and the time constant is named $T2^*$.

Clearly, $T1$, $T2$ and spin density give information about the tissue or a chemical compound under examination. In order to create images, an RF pulse sequence has to be applied by the transmit coils. There are various RF sequences targeting to extract a specific feature of the tissue, here some basic ones are summarized to give a notion. RF pulses simply change the orientation of the net magnetization vector and also used to re-phase the dephased magnetic moments of the nuclei. There are certain timing parameters for the sequences applied. TR, repetition time indicates the time between two consequent RF sequences. For example for spin density measurement before another RF pulse is applied to the system it is meaningful to wait for the net magnetization vector to return to its initial condition so that the received signal from the tissue is maximized. Though it is not mandatory to do so, if we can decode the received signal. In so called spin-echo RF sequence a 90° pulse is transmitted followed by a 180° pulse. The latter pulse rephases the dephased magnetic moments of the nuclei while they are precessing on the XY-plane. A signal is transmitted after a certain time which is TE, time-to-echo. In this time window RF coils change their functionality

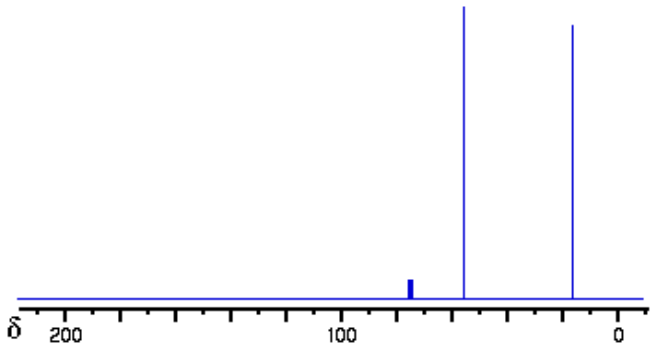

Figure 1.6. NMR spectrum of Ethanol (CH_3CH_2OH) with Carbon-13 Spectroscopy

from being transmit coils to being receive coils, and this time window happens to be handy in practice. Just like the spin-echo sequence the so called inversion recovery sequence detects spin-echo pulses emitted from the tissue. In addition to the spin-echo sequence a 180° pulse is introduced to flip the net magnetization vector to the $-z$ axis. After a certain time a 90° pulse is applied. The time window between the first 180° pulse and the following 90° pulse is called the Inversion-Delay time, TI.

1.2.2.2. Back projection. The RF excitation results in a RF signal emitted from the mass under examination. When we apply Fourier transformation to the signal we obtain the frequency spectrum of the signal. The peaks in frequency spectrum can than be mapped to certain nuclei and interaction between them(Figure 1.6). NMR uses this principle to examine material. Clearly a one dimensional Fourier analysis gives us the compounds of the material but doesn't represent any information of location. To extract location information a slice selection operation takes place first by creating an additional magnetic field with a linear gradient on static magnetic field B_0. So that the material experiences a magnetic field in different strengths over the direction of the gradient field. That way a frequency encoding has been done along the gradient field. Now we can excite a slice by transmitting an RF wave at the Larmor frequency corresponding to that slice. A spatial encoding is achieved, such that we will have peaks at different frequencies even for the same material at different positions. Those positions will be encoded along the direction of the gradient field which corresponds

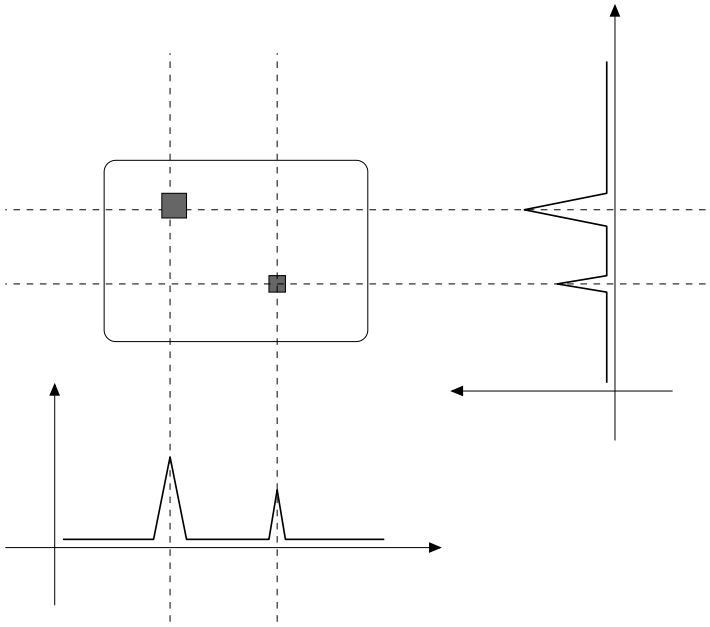

Figure 1.7. Spatial encoding and back projection

to one axis. Changing the direction of the gradient field we can scan through other axis and obtain a 2D image of the material by back projecting the spectrums obtained during these scans (Figure 1.7). In this method actually two gradient fields are applied simultaneously and rotated from acquisition to acquisition, hence it is a time consuming method to generate images.

1.2.2.3. 2D Fourier Transform. A more advanced scenario uses 2D Fourier transformation to create an image of a slice. Likewise for spatial encoding creation of images requires gradient fields. Whereas with Fourier transformation, a slice is selected with frequency encoding and the slice is scanned line by line by phase encoding. This method is applied usually in modern MRI systems.

1.3. Outline

The rest of the thesis is organized as follows, in the following chapter power conversion stage for the localization system is explained; design considerations are dis-

cussed and simulation results are given. In Chapter 3, design and evaluation of the receive antenna is presented. In Chapter 4 a low noise amplifier design is introduced. The fifth and final chapter concludes the work and talks about possible future directions.

2. Power Generation

Although MRI systems are said to be safe for the patient, there are certain risks for patients with implants. [1] reviews interactions of magnetic fields in MRI systems with implants. Besides the forces magnetic fields create on ferromagnetic implants, tissue heating is a problem even for the non-ferromagnetic implants. In [1] it is noted that rises in temperature between 16 °C to 18 °C was observed for different implants. The problem of heating was also addressed in [2], which explains a method to create a safety index for medical implants and describes the methodology and proposes to use regulatory guidelines.

To deal with the heating problem in MRI, in [3] use of fiber optic lines for receive coil interconnection especially in phased array receiver systems is discussed. [4] further discusses the similar needs for changing coaxial cables with their fiber-optic counterparts in interventional tools. Similarly in [5] a system is introduced with optical power and data transfer for interventional operations which emphasizes risks of patient safety and heating in conventional coaxial wires due to RF emissions.

In our front-end design all links to the external environment are decided to be over optical links due to the risks mentioned in literature. As risks do exist for other implants, batteries cannot also be used in an interventional device. Power of the front-end device is supplied over an optical link to the device from a laser. Following section summarizes design considerations for electrical power conversion by means of system design and efficiency. A charge pump design is explained in the next section for boosting input voltage level to the desired level.

2.1. Charge Pump

2.1.1. Introduction

Charge pumps are generally used to obtain higher voltages from a voltage source, which is supplied by the external system. Typical applications are to use the charge pump to generate 10-15V of voltage to drive internal flash memory cells from a voltage about 3-5V set by power supply. The structure is also popular in passive RFID tags to generate a supply voltage from the voltage signal on the receiver antenna. Our aim is also to generate a DC supply voltage from an incoming alternating voltage with the use of charge pumps.

2.1.2. Theory

2.1.2.1. Cockcroft-Walton Charge Pump. Charge pumps elevate the voltage that they are working with. A simple representation is given in Figure 2.1 to explain the operation. As seen in the figure, there are two switches across the capacitor controlled by a signal. In the first phase of operation, capacitor is charged to the input voltage V_{In}. At the end of first phase, output voltage is equal to the input voltage and some charge has been stored in the capacitor. In the second phase, as switches change their state, the output voltage is elevated to a voltage $V_{In} + V_C$ and under no load condition becomes $2 * V_{In}$. To further increase the output voltage with respect to the input capacitor stage can be cascaded as in Figure 2.2. This topology was first proposed by Cockcroft-Walton and named after them.

With this basic operation high voltages could be generated. However, this design is not efficient in an integrated design, due to the parasitic capacitances, and output resistance of the voltage multiplier increases with the number of stages added.

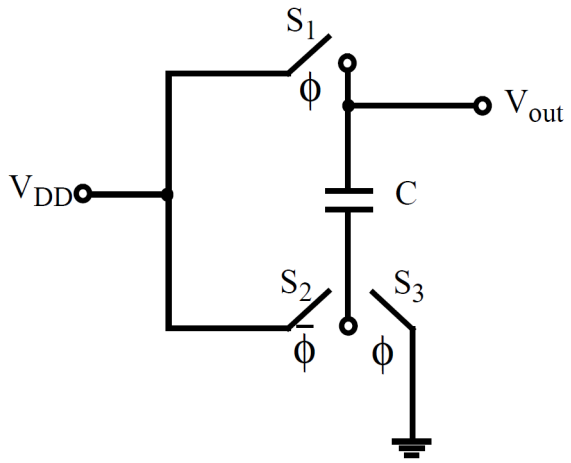

Figure 2.1. Operation of voltage doubler

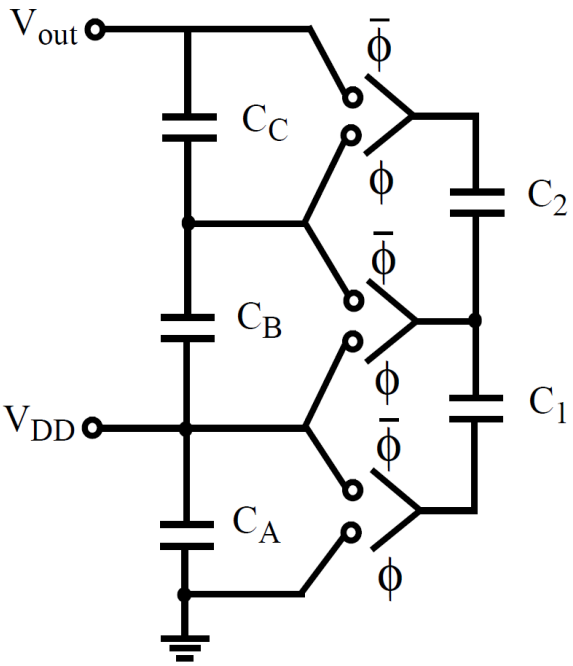

Figure 2.2. Cockcroft-Walton Charge Pump

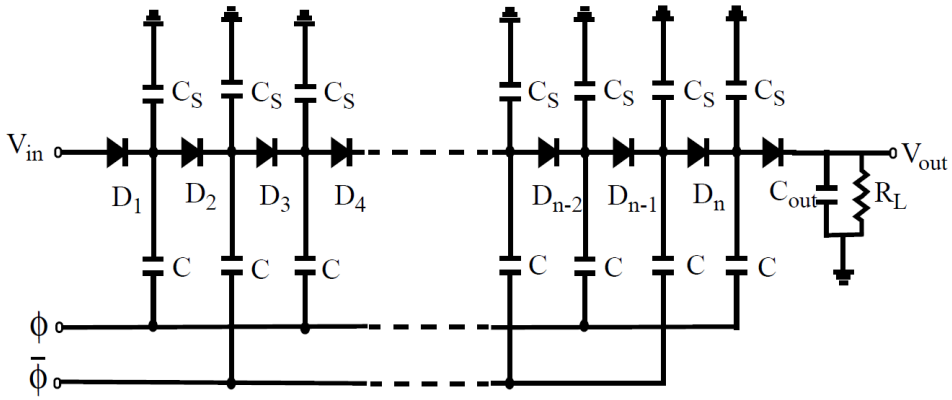

Figure 2.3. Dickson Charge Pump

2.1.2.2. Dickson Charge Pump. Another widely used topology is the Dickson charge-pump seen in Figure 2.3. There are two clocks in the circuit with amplitude V_Φ, which are non-overlapping and have 180° phase difference. When clock with phase Φ is at 0V the first diode passes charges until the first node is $V_{in} - V_{th}$ where V_{th} is the threshold voltage of the diode. As the clock rises to V_Φ the first node's potential rises together to $(V_{in} - V_{th}) + V_{Phi}$. As the voltage at the second node goes to 0V by this change, the second diode starts conducting, till second node voltage becomes $(V_{in} - V_{th}) + V_{Phi} - V_{th}$. When the clock with phase Φ goes low once again second node voltage becomes $V_{in} + 2(V_\Phi - V_{th})$, after N stages of diodes the output voltage is,

$$V_{out} = V_{in} + N(V_\Phi - V_{th}) - V_{th} \tag{2.1}$$

2.1.3. Design Considerations

Some points should be considered when designing a charge pump for an optimized design for the specific application. Output voltage level is one such parameter that should be determined, simply charge pumps are build using certain voltage doubler cell topologies and output voltage determines the stage count of the total topology. In our design the output voltage is about 3V to drive a light emitting diode. Current

drivability is another factor to be determined. Together with the output voltage it determines the output power of the topology. In our design, this parameter is not fixed strictly, basically the much drive current the better the design is. Usually output ramp-up time is another parameter that should be considered, but in our design this value is not constrained. Lastly power consumption of the charge pump is an important parameter, since it is a part of the power generation block it shouldn't use the available input power.

2.2. Design

2.2.1. Charge Pump

Schematic of the designed charge-pump is shown in Figure 2.4 for a single stage. In Figure 2.5 the overall topology for power generation is represented. For the single stage there are two diode connected pmos devices and two on-chip capacitors. The bulk terminal of the mos devices are connected to the drain terminal, that is because the drain terminal is usually at a higher voltage level and this way leakage from the bulk is minimized. Shown topology requires an ac swing at the input; for one phase input capacitance is charged to a certain level, in the next phase of the input signal the diode connected mos at the reference voltage is open and further charges the capacitor. This charges than shifted to the output capacitor over the diode connected mos at the output.

This simple operation is effected by the capacitance values and W/L ratios of the transistors. The capacitors can be made larger for a better operation(which increases the ramp-up time, but not an issue for our design), however this approach is not possible after a certain size when chip area is a concern. After performing some simulations, those values are fixed at 3pF for each capacitor. MOS devices have a limited drive capability. Thus, bigger device sizes are required to make the output drive capability

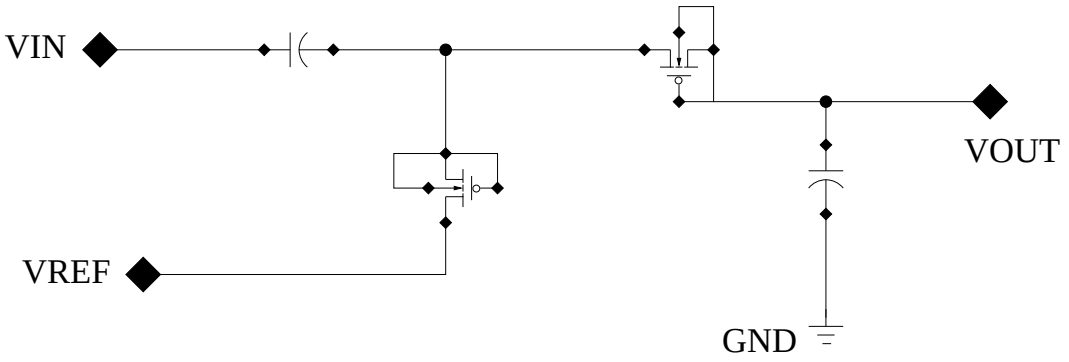

Figure 2.4. Charge pump schematic for a single stage

higher. Having big transistors in turn increases the power consumption of the charge pump circuit. In our design the input signal swings at a frequency of 100MHz and there is a leakage current to the bulk terminal increasing with the frequency. Another point is the parasitic capacitances of the mos devices. Increasing parasitic capacitances negatively impact the charge pump efficiency. The channel width for mos devices are chosen to be 50um, where the devices have the shortest channel length of 0.18um.

Two charge pump stages are used to generate the output voltage. More stages can be added to the design if higher output voltages are desired. This once again will have a negative impact on the power consumption of the charge pump circuit.

2.3. Results

Following plots show the performance of the designed charge pump circuitry. In Figure 2.6 plots are given for different load conditions.

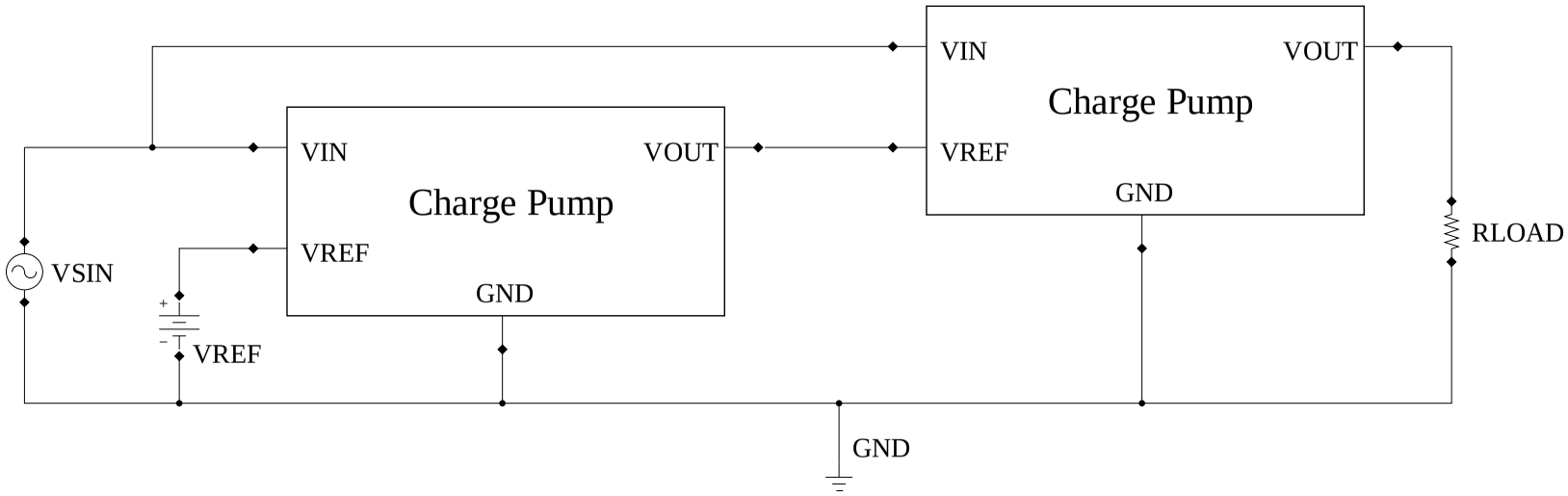

Figure 2.5. Power conversion circuit



Figure 2.6. Output potentials under different load resistances

3. Receive Antenna

3.1. Design and Simulation

A coil intended to be used at 63.6MHz is designed using a 3-D Wave solver, and S-parameters are extracted for frequencies 60-70MHz. Impedance of the coil is calculated using the admittance parameters matrix extracted from the 3-D wave solver. A matching network is designed to match the coil to 50ohm load impedance with minimum loss. Therefore, a minimum number of elements are used for the matching network. To satisfy maximum power transfer to the load, conjugate matching is made. The process is carried for different coil sizes which are $1mm$ x $1mm$, $1.5mm$ x $1.5mm$, $2mm$ x $2mm$ and $3mm$ x $3mm$ in diameter. The designs are then simulated along with the matching topology and the load. Following figures show the simulated topologies and the results respectively.

In addition, different geometries are also examined in order to find a matching coil whose Q^2xR value is near 1500Ω and can be realized with the technology at hand. This design is required to realize an input amplifier topology with so called resonant matching. In contrast to simultaneous noise and power matching, resonant matching boosts the input signal voltage with the help of resonant tank formed by the coil and an added capacitor. Even there is no power matching between the input stage of the amplifier and the receiver antenna, noise figure of the system is calculated to be lower at frequencies of interest.

3.1.1. Geometrical model

The coil is first drawn according to the process technology at hand. The drawings include the FR4 substrate and its physical properties. The environment that the coil is air. Different turn counts were simulated first for each coil and the turn count

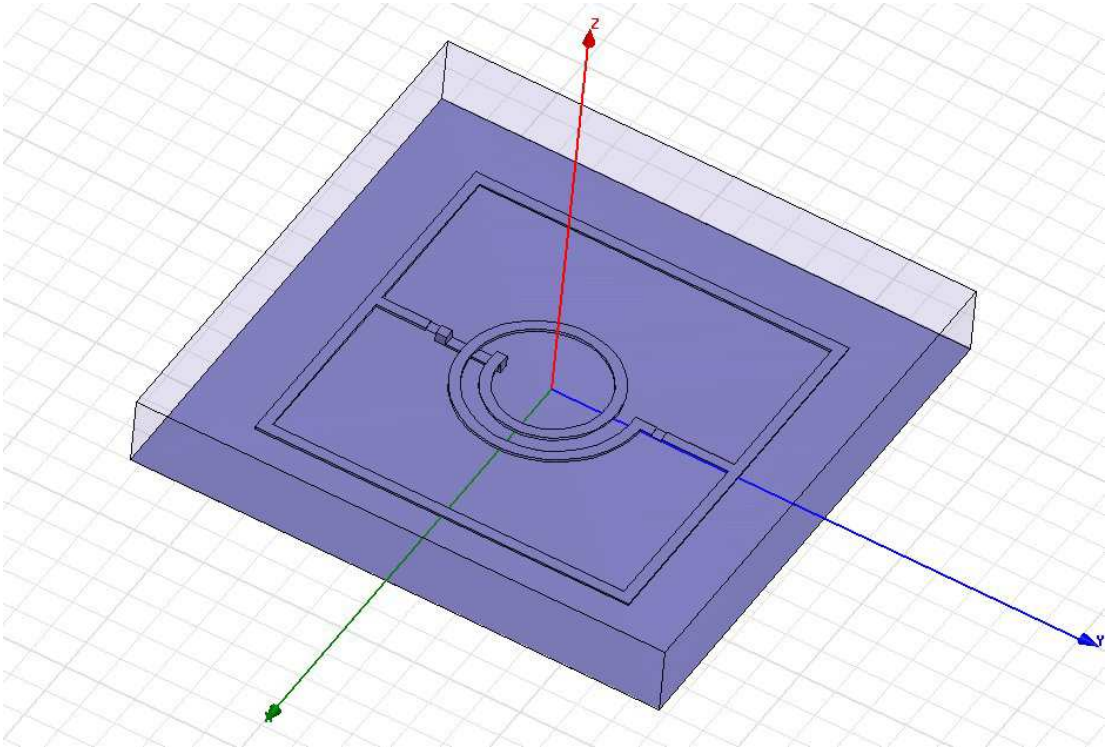

Figure 3.1. 3-D view for $1mm$ x $1mm$ coil with 1.5 turn

maximizing the quality factors were determined. As the turn size increase the resistance of the coil increases as well together with its reactive component values. This results a rise in quality factor up to a point where the inner circle is filled with the conducting coil and degrades the reactive component. In Figures 3.1,3.2,3.3,3.4 drawn coils with sizes $1mm$ x $1mm$, $1.5mm$ x $1.5mm$, $2mm$ x $2mm$ and $3mm$ x $3mm$ are shown respectively. As can be seen in the figures the turn counts vary with different coil sizes, which maximizes the quality factors.

In Table 3.1 the quality factors of the drawn coils together with their impedances at $63.5MHz$ are given. Together with these results s-parameters are also extracted to be used as electrical models for the coils in the following simulations for matching.

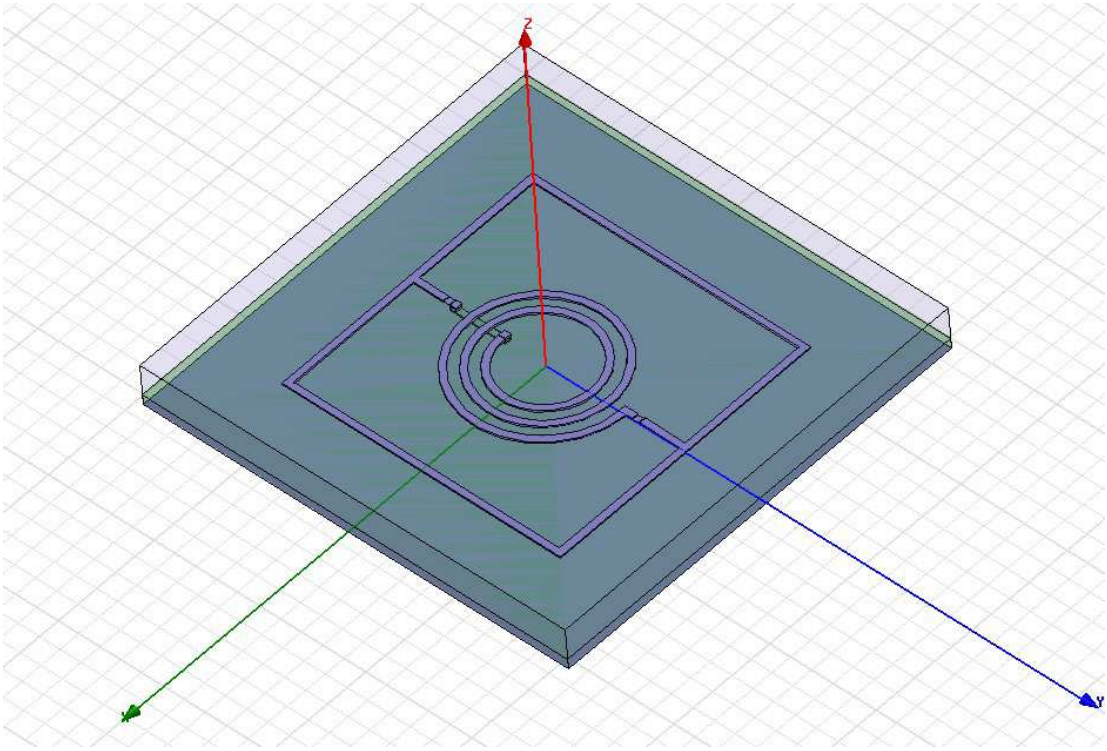

Figure 3.2. 3-D view for 1.5mm x 1.5mm coil with 2.5 turn

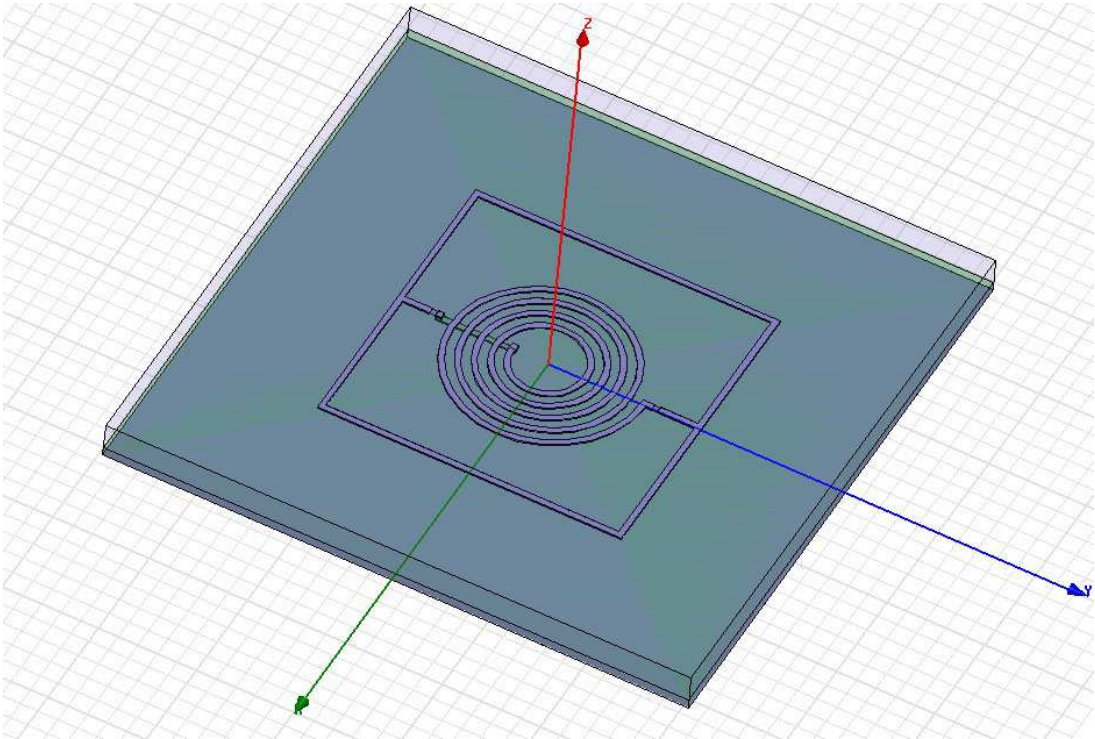

Figure 3.3. 3-D view for 2mm x 2mm coil with 4.5 turn

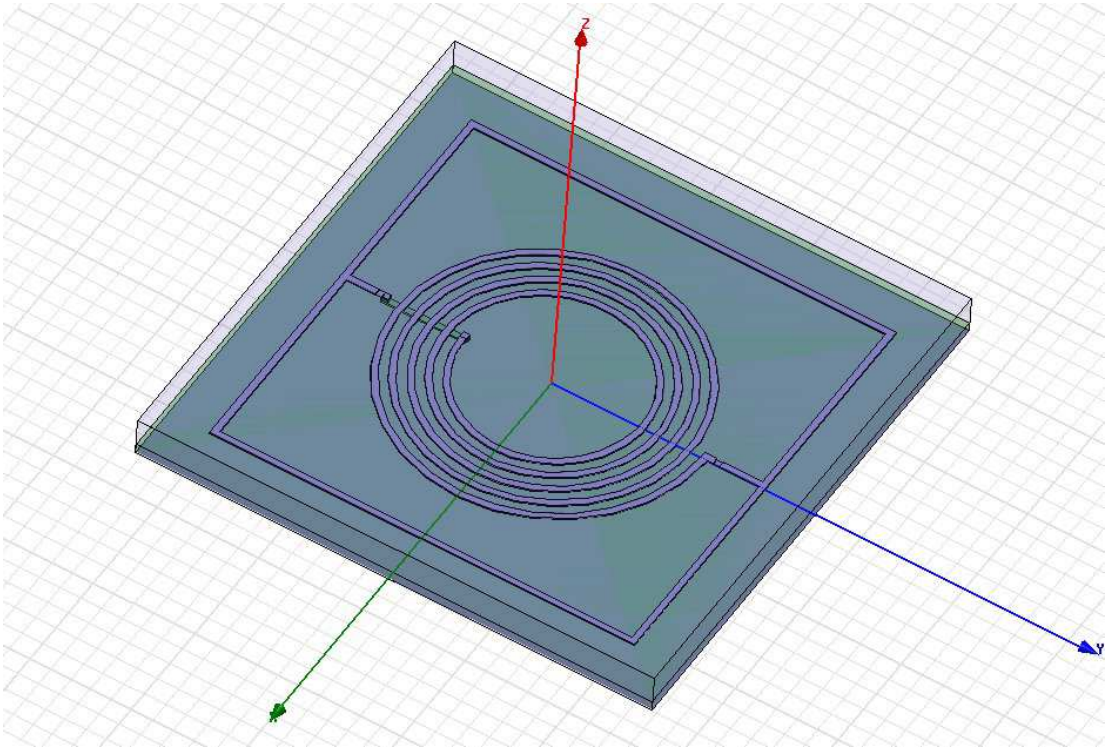

Figure 3.4. 3-D view for $3mm$ x $3mm$ coil with 4.5 turn

3.1.2. Matching

With the use of a 3-D solver electrical models of the coils are extracted. The coils need to be matched to 50Ω in order to make s-parameter analysis after production. The matching network seen in Figure 3.5 is used for all coils, which happened to be sufficient. The values for the L-network is presented in Table 3.2.

An AC analysis is made to measure power gain at the output. The antenna is modeled with an independent source connected to represent the induced wave as seen in Figure 3.5. In Figures 3.6, 3.7, 3.8 and 3.9 the results of the AC analysis is shown for the coil sizes $1mm$ x $1mm$, $1.5mm$ x $1.5mm$, $2mm$ x $2mm$ and $3mm$ x $3mm$ respectively.

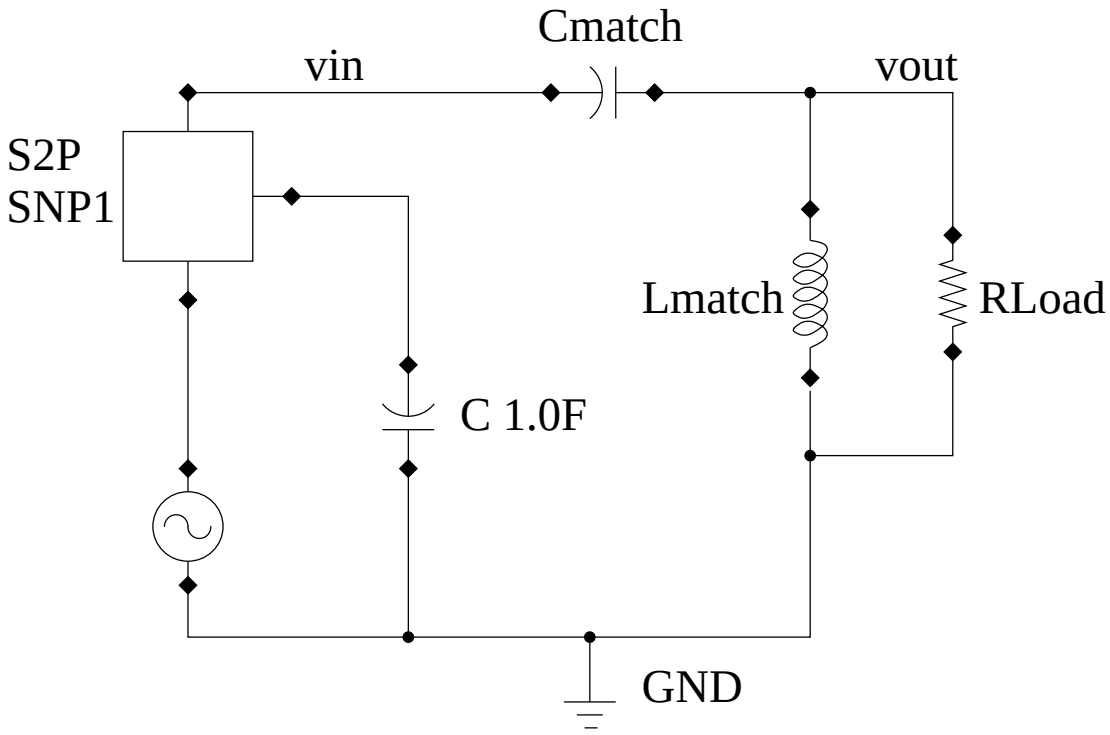

Figure 3.5. Schematic for ADS AC Analysis

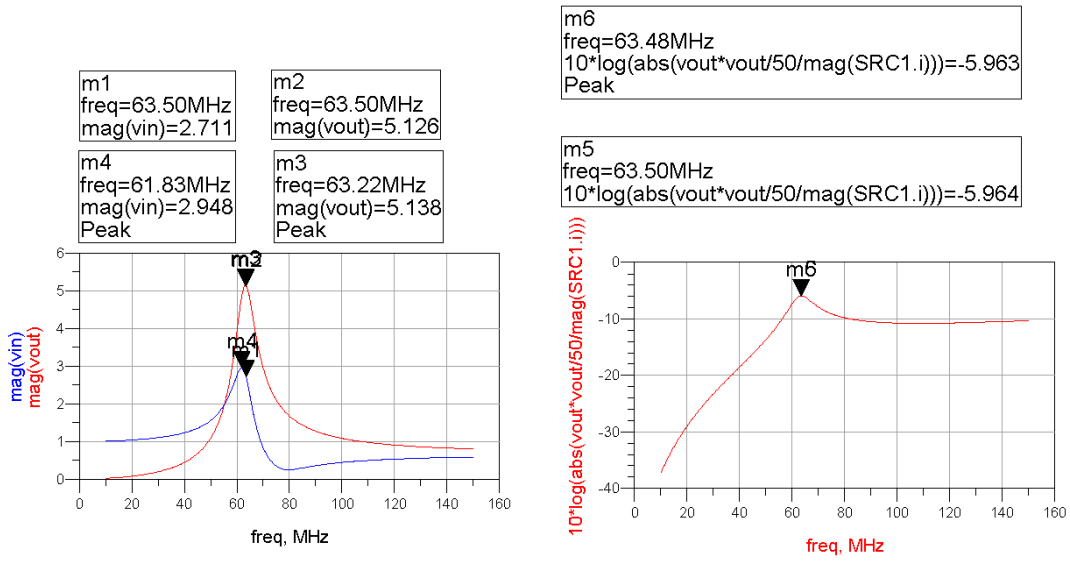

Figure 3.6. AC analysis results for $1mm$ x $1mm$ coil

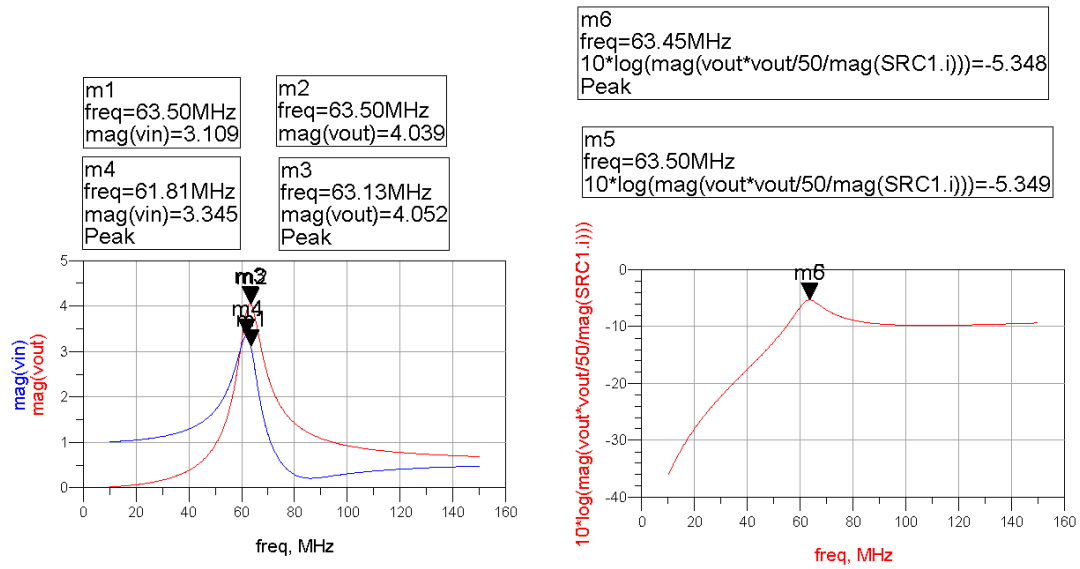

Figure 3.7. AC analysis results for $1.5mm$ x $1.5mm$ coil

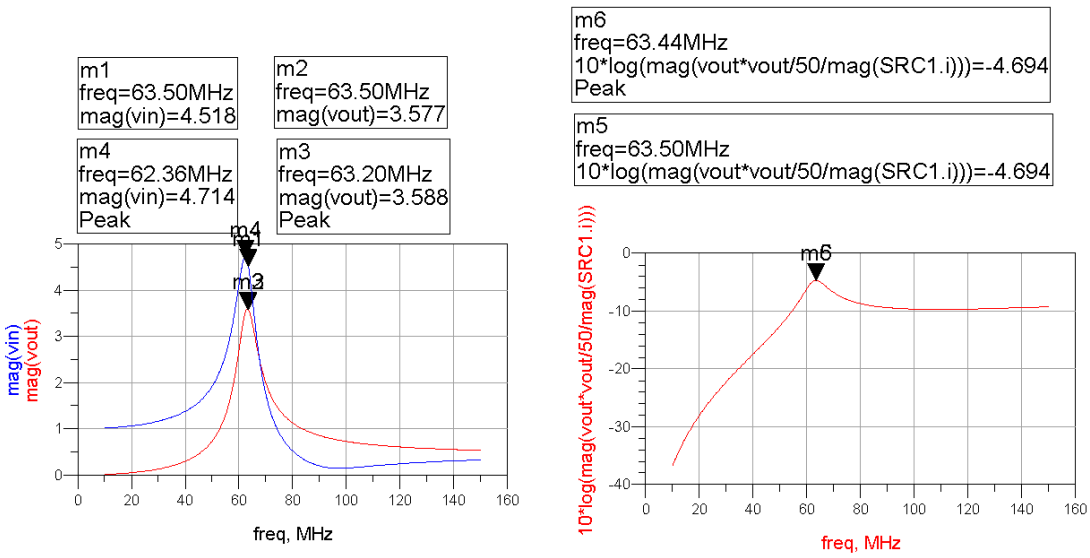

Figure 3.8. AC analysis results for $2mm$ x $2mm$ coil

Table 3.1. Simulated impedance and quality factor values

Coil Dimensions	Impedance [Ω]	Quality Factor
$1mm$ x $1mm$	$0.1107 + 1.3j$	11.7267
$1.5mm$ x $1.5mm$	$0.2564 + 2.8014j$	10.9218
$2mm$ x $2mm$	$0.53 + 6.0625j$	11.4415
$3mm$ x $3mm$	$0.901 + 10.6418j$	11.8240

Table 3.2. Simulated component values for the matching network

Coil Dimensions	Capacitance [pF]	Inductance [nH]
$1mm$ x $1mm$	686.7	5.903
$1.5mm$ x $1.5mm$	393.3	8.997
$2mm$ x $2mm$	224.1	12.97
$3mm$ x $3mm$	144.9	16.98

An s-parameter analysis is also conducted, the circuit used for simulation is presented in Figure 3.10. Since this network is a one port network S_{11} is the only s-parameter and represents the matching of the design. In Figures 3.11, 3.12, 3.13 and 3.14 S_{11} is plotted against the targeted frequency range for coil sizes $1mm$ x $1mm$, $1.5mm$ x $1.5mm$, $2mm$ x $2mm$ and $3mm$ x $3mm$ respectively.

3.1.3. Resonant Coil

In [6] a technique is introduced to convey NMR signals, which have little amplitude in nature. The so called resonant matching approach requires a resonant tank formed by the input receiver antenna and an added capacitor. For an efficient design the Q^2xR product of the coil should be 1500Ω. With the technology at hand the design space is swept with coil spacing and width. In table 3.3 coil spacing is swept for $60um$ line width. In table 3.4 again coil spacing is swept but this time for $30um$ line width. In Table 3.5 line width is swept along with line spacing such that the length of the coil is not affected. In Table 3.6 line width is swept where line spacing is constant and is

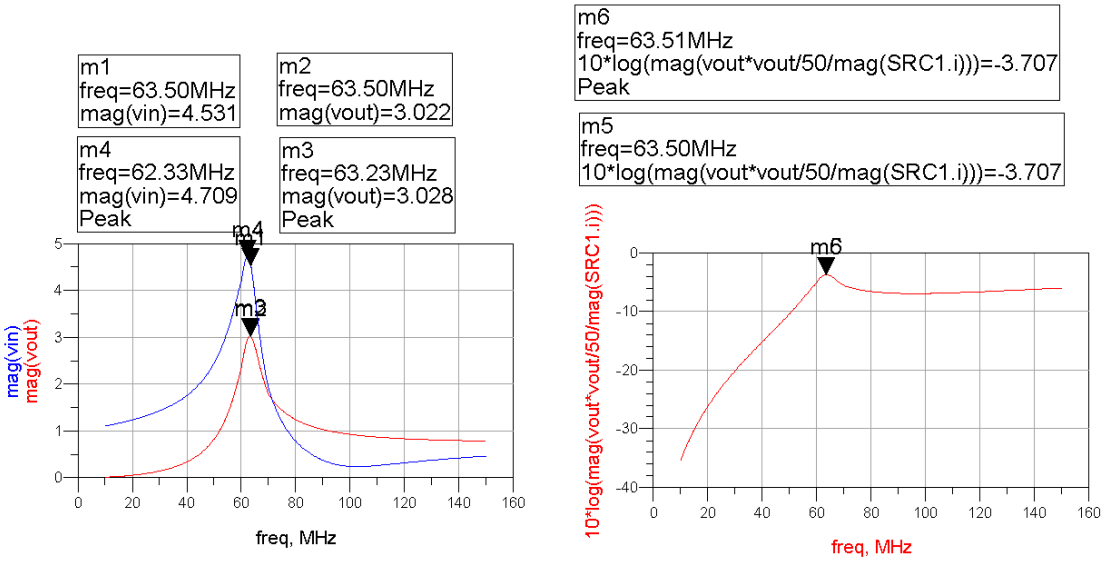

Figure 3.9. AC analysis results for $3mm$ x $3mm$ coil

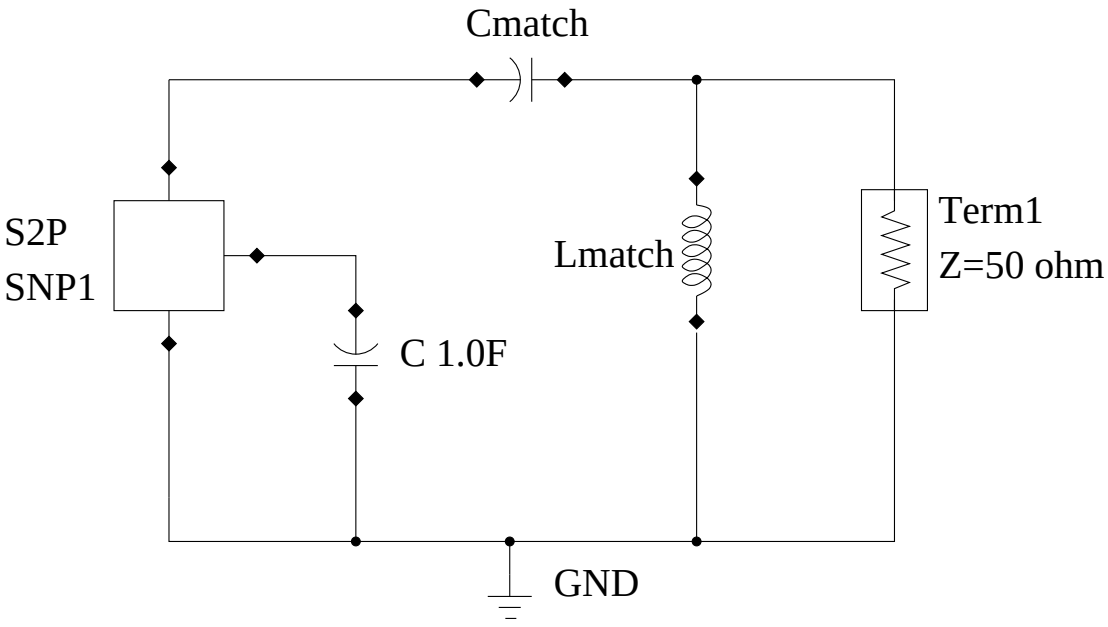

Figure 3.10. Schematic for ADS S-Parameter Analysis

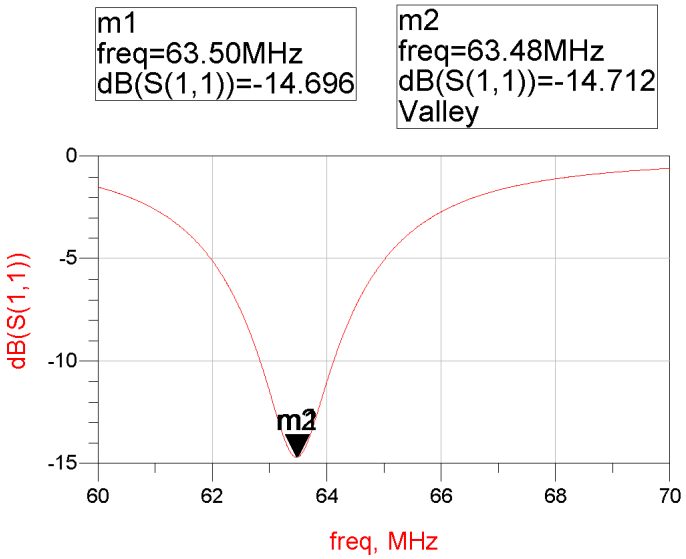

Figure 3.11. Simulated S_{11} for $1mm$ x $1mm$ coil

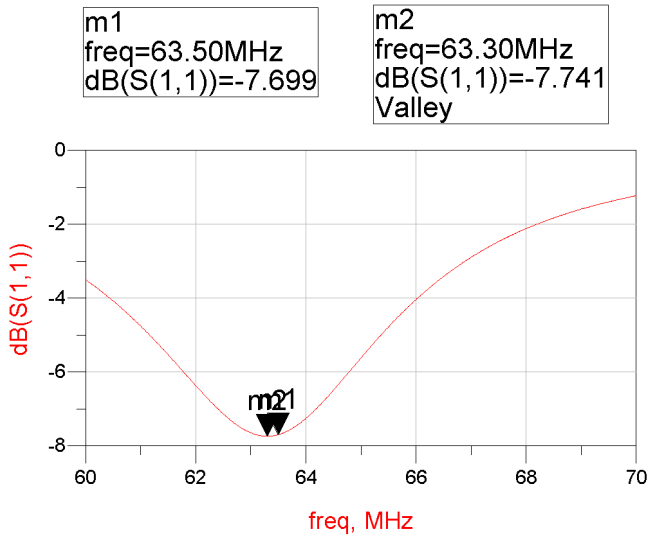

Figure 3.12. Simulated S_{11} for $1.5mm$ x $1.5mm$ coil

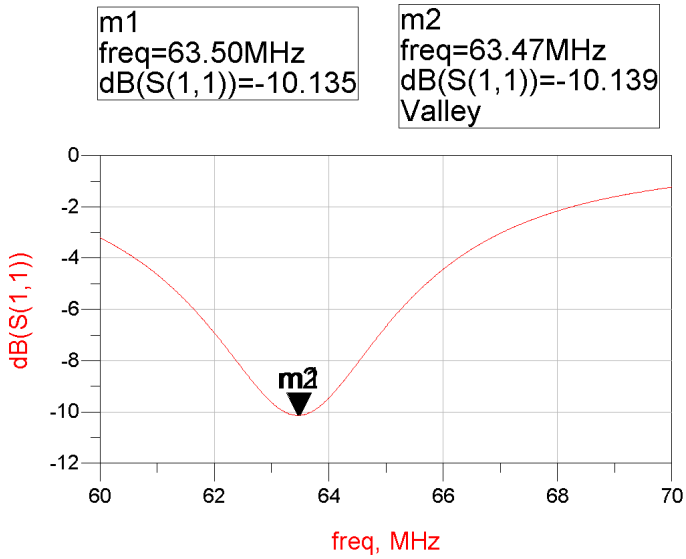

Figure 3.13. Simulated S_{11} for $2mm$ x $2mm$ coil

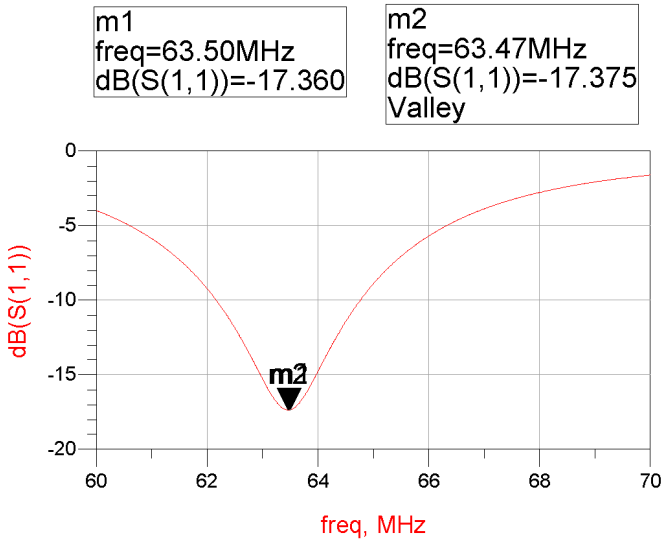

Figure 3.14. Simulated S_{11} for $3mm$ x $3mm$ coil

$90um$.

Table 3.3. Simulated Q^2xR values for $3mmx3mm$ coil with 4.5 turns, $60um$ line width

Line spacing $[um]$	Line width $[um]$	Q	R [Ω]	Impedance [Ω]	Q^2xR [Ω]
90	60	11.79	0.899	$0.899 - 10.631j$	124.96
70	60	12.4099	0.955	$0.955 - 11.8133j$	147.07
50	60	13.0426	0.995	$0.995 - 13.0647j$	169.25

Table 3.4. Simulated Q^2xR values for $3mmx3mm$ coil with 4.5 turns, $30um$ line width

Line spacing $[um]$	Line width $[um]$	Q	R [Ω]	Impedance [Ω]	Q^2xR [Ω]
120	30	7.6825	1.5684	$1.5684 - 12.005j$	92.56
90	30	7.36	1.5938	$1.5938 - 11.716j$	86.33
70	30	8.04	1.686	$1.686 - 13.507j$	108.98
50	30	9.98	1.7737	$1.7737 - 17.5512j$	176.66

It is seen from the Table 3.3 and Table 3.4 with decreasing line spacing quality factor of the coil increases. Resistance of the coil also increases due to the slight increase in the length of the coil. As a result we obtain higher Q^2xR product with decreasing line width.

Table 3.5. Simulated Q^2xR values for $3mmx3mm$ coil with 4.5 turns

Line spacing $[um]$	Line width $[um]$	Q	R [Ω]	Impedance [Ω]	Q^2xR [Ω]
90	60	11.79	0.899	$0.899 - 10.631j$	124.96
100	50	10.6319	1.04	$1.04 - 11.013j$	117.55
110	40	9.2422	1.2315	$1.2315 - 11.441j$	105.19
120	30	7.6825	1.5684	$1.5684 - 12.005j$	92.56

Table 3.6. Simulated Q^2xR values for $3mmx3mm$ coil with 4.5 turns, $90um$ line spacing

Line spacing $[um]$	Line width $[um]$	Q	R [Ω]	Impedance [Ω]	Q^2xR [Ω]
90	60	11.79	0.899	$0.899 - 10.631j$	124.96
90	50	10.17	0.9921	$0.9921 - 10.065j$	102.61
90	40	8.8665	1.2122	$1.2122 - 10.7801j$	95.30
90	30	7.36	1.5938	$1.5938 - 11.716j$	86.33

From Table 3.5 and Table 3.6 we can deduce by looking at the impedance column that resistance increases with decreasing line width as expected. Whereas inductance values stay almost the same, hence quality factor decreases. When we generalize this information, we can deduce that for maximizing Q^2xR product we should decrease the line spacing and increase the line width. But one should keep in mind that the area is constraint and the simulations were done for constant turn counts. When we want to use as much of the area as possible to increase the inductance we should decrease the line width also. For $3mmx3mm$ a coil is drawn and simulated for maximizing Q^2xR product, other coils are simulated for $4mmx4mm$ dimensions. The results are given in Table 3.7

Table 3.7. Simulated Q^2xR values for higher turn numbers

Dimensions	Line Spacing $[um]$	Line Width $[um]$	Q	Impedance [Ω]	Turn count	Q^2xR [Ω]
$3mmx3mm$	30	30	14.5804	$6.1255 - 87.2894j$	20.5	1302.2
$4mmx4mm$	90	60	11.9887	$2.1551 - 25.862j$	10.5	309.75
$4mmx4mm$	90	60	11.8401	$2.2366 - 26.7672j$	11.5	313.54
$4mmx4mm$	30	30	12.0423	$12.1555 - 141.8152j$	21.5	1762

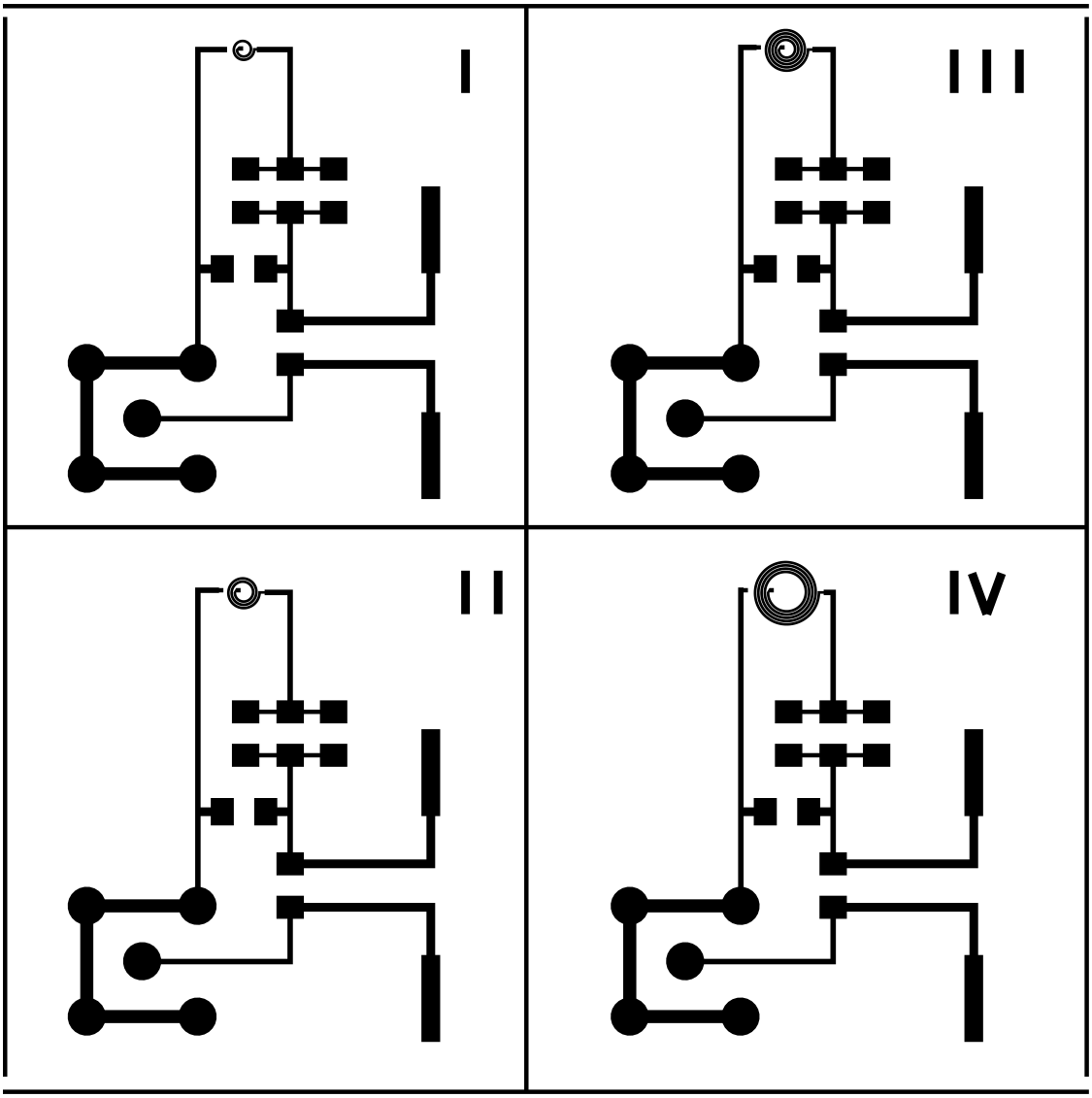

Figure 3.15. Layout for coils

3.2. Fabrication and Measurements

A layout for printed circuit board production is drawn, the layout is shown in Figure 3.15. Although our simulations show that an L-network is sufficient for matching, extra pads are added to the layout to fine tune matching network for the variations in actual discrete component variation.

The resulting coils are than measured using a spectrum analyzer and matching

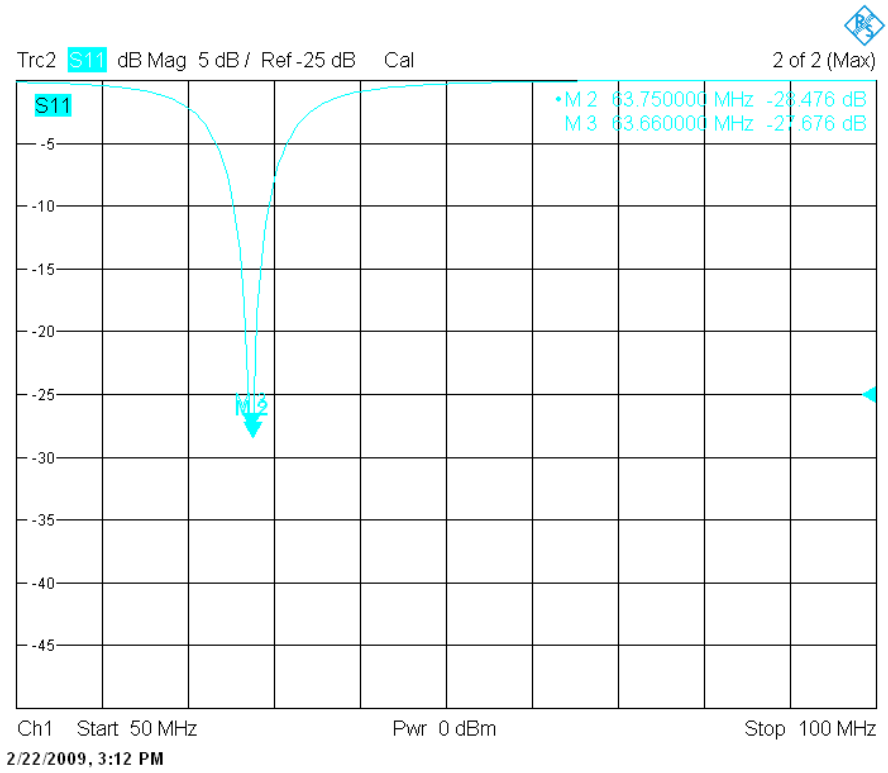

Figure 3.16. Measured S_{11} for $1mm$ x $1mm$ coil

components were placed with practical iterations around the simulated values. In Figures 3.16 and 3.17 measured S_{11} values for $1mm$ x $1mm$ and $3mm$ x $3mm$ sized coils are presented in a rectangular plot. The smith chart representations are shown in Figure 3.18 and Figure 3.19.

Measured values for $1mm$ x $1mm$ and $3mm$ x $3mm$ sized coils are listed also in Table 3.8.

Table 3.8. Measured impedance and S_{11} values

Coil Dimensions	Impedance [Ω]	$S_{11}[dB]$
$1mm$ x $1mm$	$52.551 - 3.417j$	-27.67
$3mm$ x $3mm$	$52.004 - 1.0921j$	-33.39

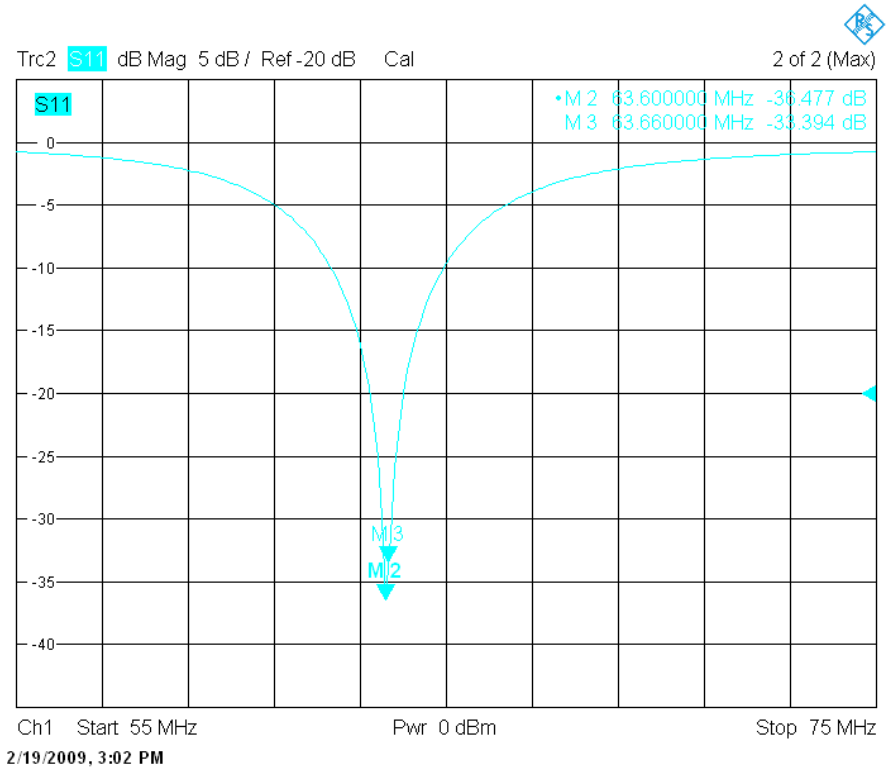

Figure 3.17. Measured S_{11} for $3mm$ x $3mm$ coil

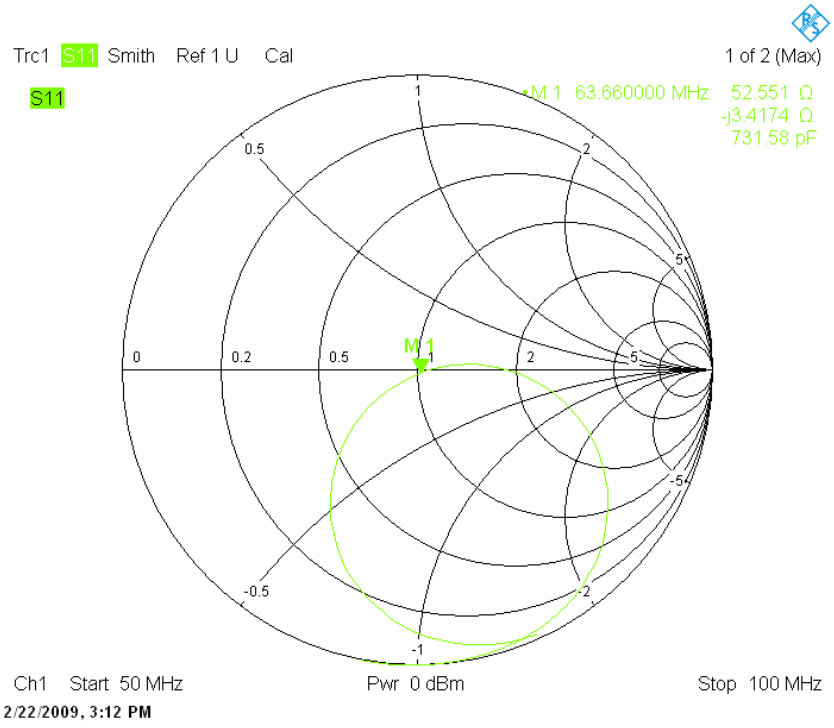

Figure 3.18. Measured S_{11} on smith chart for $1mm$ x $1mm$ coil

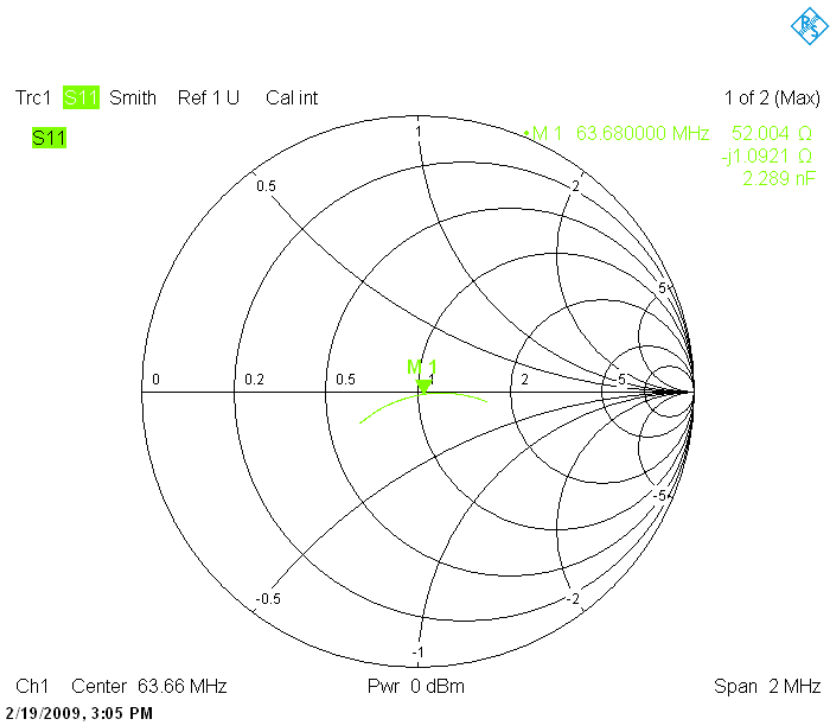

Figure 3.19. Measured S_{11} on smith chart for $3mm$ x $3mm$ coil

4. Low Noise Amplifier

4.1. Introduction

The first block in most wireless receivers is typically a low noise amplifier (LNA), which is responsible for providing enough gain to overcome the noise of the subsequent blocks and its noise figure sets a lower bound on the noise figure of the whole system [7]. Moreover for high linearity the LNA should amplify signals whose amplitude varies from few nV to tens of mV without any significant distortion. Additionally, sensitivity of the LNA determines the sensitivity of the whole receiver, which is defined as the minimum level of the input signal for which the receiver provides an acceptable signal quality. Furthermore, LNAs are usually preceded by passive filters in order to impose the required input impedance and filtering the undesired signals.

Minimum noise figure can be obtained from a given device by using the optimum source impedance. However, this approach is insufficient because the source impedance that minimizes the noise figure generally differs from the impedance that is required by the preceding stage which maximizes the power gain. This may result in an LNA having a bad input matching hence poor gain and good noise figure or vice versa. As summarized briefly there are many points to consider like voltage gain, input matching, power consumption and linearity simultaneously in an LNA design. In this chapter common LNA practices are summarized and designed LNA architecture together with simulation results are presented.

4.2. Theory

4.2.1. Noise

Noise is the essential factor that limit the sensitivity of a communication system. A classical definition of noise is everything except the desired signal. More formally noise is a random process and cannot be defined a specific value at a particular time [7]. Hence, statistically derived equations are used in order to define noise like spectral density.

Noise is basically examined in two categories which are interference noise and inherent noise. Interference noise is due to unwanted interaction between the circuit and the different parts of the circuit itself. Power supply noise or electromagnetic interference between wires are the two most known sources of interference noise. This kind of noise can be significantly reduced by using appropriate circuit wiring or layout techniques.

Inherent noise is a result of fundamental properties of the devices and circuits, and is related to random noise signals which can just be reduced. Inherent noise is only moderately affected by circuit wiring or layout, such as using multiple drain contacts or multiple gate transistors to change the resistance value of the drain or gate of a MOSFETs. The dominant inherent noise sources in integrated circuits are thermal noise, shot noise and flicker noise.

4.2.1.1. Thermal Noise. Thermal noise is caused by the random motion of the charge carriers in a conductor. The power spectrum density of the thermal noise is exactly proportional to the absolute temperature due to the thermal origin and given by,

$$P_N = kT\Delta f \tag{4.1}$$

where k is the Boltzman constant, T is the absolute temperature in °K, and Δf is the bandwidth of the noise measured in Hz. Thermal noise shows the same spectral power density over all frequencies, hence it is a white noise source in electronic circuits.

4.2.1.2. Shot Noise. Shot noise is mainly caused by random flow of carriers through a potential barrier. It is first described by Schottky and is also referred as Schottky noise. Shot noise happens when there is a direct current flow over a potential barrier [7]. It is inherent to nonlinear devices such as diodes and transistors. Shot noise does not change with temperature, rather with the current flow and the bandwidth as given by,

$$\overline{i_n^2} = 2qI_{DC}\Delta f \tag{4.2}$$

where $\overline{i_n^2}$ is the rms noise current, q is the charge of an electron in coloumb, I_{DC} is the DC current in amperes, and Δf is the noise bandwidth in hertz. Shot noise is also a white noise source like thermal noise.

4.2.1.3. Flicker Noise. Flicker noise has not been identified very well. It seems to come from the macroscopic defects of the materials; therefore it describes the quality of the conductive medium. The power spectral density of flicker noise is inversely proportional to the frequency hence it is also called $1/f$ noise or pink noise. Flicker noise does not depend on temperature but rather proportional to the current. Flicker noise is caused by randomly trapping and releasing of the charges in the defects and impurities of the channel region in MOS devices [7]. The excess energy levels at the point that silicon crystal and gate oxide emerge can randomly trap and release charges. Larger MOSFETs exhibit less flicker noise due to the smoothing effect of the large gate capacitance. Furthermore, MOSFETs inherently exhibit more flicker noise in comparison to bipolar devices which are lateral. The spectral density of flicker noise

for FETs is given by,

$$\overline{i_n^2} = \frac{K}{f}.\frac{g_m^2}{WLC_{ox}^2}.\Delta f \tag{4.3}$$

where K is a device-specific constant, g_m is the transconductance of the FET, f is the operating frequency, C_{ox} is the gate-oxide capacitance per unit area, and W and L are the width and length of the FET device, respectively and Δf is the noise bandwidth in hertz.

Noise performance of a circuit is usually characterized by a parameter called noise factor(F) or noise figure (NF) that represents how much the given system degrades the signal-to-noise ratio. Noise factor for a system is given by,

$$F = \frac{Total\ output\ noise\ power}{Output\ noise\ power\ due\ to\ input\ noise} = \frac{SNR_{out}}{SNR_{in}} \tag{4.4}$$

Noise figure is simply related to the noise factor by,

$$NF = 10logF \tag{4.5}$$

In a cascaded system, as the receiver front-end, the total noise factor is given by the Friis equation [8],

$$F_{total} = F_1 + \frac{F_2 - 1}{G_1} + \frac{F_3 - 1}{G_1 G_2} + \frac{F_4 - 1}{G_1 G_2 G_3} + ... \tag{4.6}$$

where subscripts denotes the stages and F stand for noise factor and G stands for power gain of the stage. In a receiver front-end if the gain of the first stage (LNA) is

sufficiently high then,

$$F_{receiver} = F_{LNA} + \frac{(F_{rest} - 1)}{G_{LNA}} \tag{4.7}$$

can be noted. As can be seen from the equation noise factor of the LNA dominates the overall noise factor.

4.2.2. Noise Sources in FETs

MOS devices are fundamentally voltage-controlled resistors; therefore one should expect a thermal noise associated with the carriers in the channel similar to the noise of carriers in a conductor. The following expression for the drain current noise of MOS devices, also known as channel thermal noise, has been derived by Van der Ziel in [9],

$$\overline{i_{nd}^2} = 4kT\gamma g_{d0}\Delta f \tag{4.8}$$

where g_{d0} is the the zero bias drain conductance of the device and γ is the bias and technology dependent variable representing thermal noise.

Another thermal noise source in MOS devices is associated with the substrate resistance, R_{sub}. Since the channel to bulk capacitance C_{cb}, can be ignored at frequencies low enough, thermal noise due to substrate resistance contribute to noisy drain current by modulating the back gate potential. The relation is expressed in,

$$\overline{i_{nd,sub}^2} = \frac{4kTR_{sub}g_{mb}^2}{1 + (\omega R_{sub}C_{cb})^2}.\Delta f \tag{4.9}$$

Distributed resistance of the gate terminal generates additional noise in FETs [10]. For noise purposes; the value of this resistance is given by,

$$R_g = \frac{R_\diamond W}{3n^2 L} \tag{4.10}$$

where $R_\diamond$ is the sheet resistance of the polysilicon gate terminal, n is the number of gate fingers in the layout of the device, W is the total gate width of the device and L is gate length of the device. The factor 1/3 is the result of distributed analysis of the gate terminal that assumes each gate finger contacted at only one end. Contacting both ends results in reducing of this factor to 1/12. Therefore, by using appropriate layout techniques, the value of this resistance thus, the noise contribution of this source can be reduced significantly.

In addition to the noise sources introduced above, the thermal agitation of channel charge causes fluctuations in the channel potential that leads to a noisy gate current due to the capacitive coupling. For MOSFET devices operating in the saturation region, this extra noise was modeled by introducing a frequency-dependent gate conductance(g_g), and an equivalent gate current noise is expressed as,

$$\overline{i^2_{nd,sub}} = 4kT\delta g_g \Delta f \tag{4.11}$$

$$g_g = \frac{\omega^2 C^2_{gs}}{5g_{d0}} \tag{4.12}$$

where δ is the technology-dependent gate noise coefficient [9]. As seen in the given equations, the gate current noise power spectral density is proportional to ω, thus gate current noise is not a white noise unlike the drain current noise.

The gate current noise is partially correlated with the drain noise and their cor-

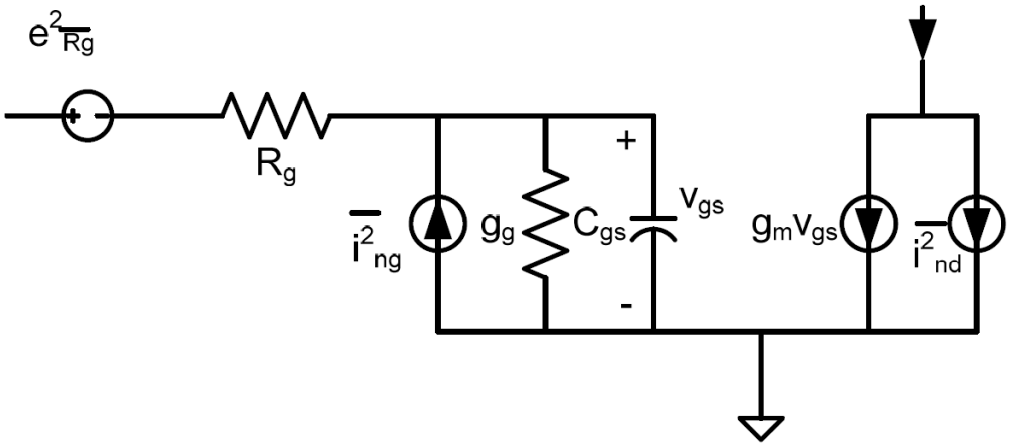

Figure 4.1. Noise sources in MOSFETs

relation coefficient is given by,

$$c = \frac{\sqrt{i_{ng} i_{nd}^*}}{\sqrt{i_{ng} i_{nd}}} \tag{4.13}$$

where c is a complex number. According to [11], for short channel MOSFET devices c is larger. The purely imaginary value of c indicates the capacitive coupling between the channel and the gate induced noise sources.

To sum up noise sources in MOSFET devices are presented briefly in Figure 4.1.

4.2.3. Noise Analysis in FETs

In order to achieve minimum noise figure, the optimum noise admittance Y_{opt} must be equal to the termination admittance, Y_s. The expressions for noise parameters F_{min}, R_n, B_{opt} and G_{opt} can be derived for a MOSFET device by considering a two-port network model for the MOSFET device shown in Figure 4.2. Here we assume that drain current noise and gate induced current noises are the dominant noise sources of MOSFET devices.

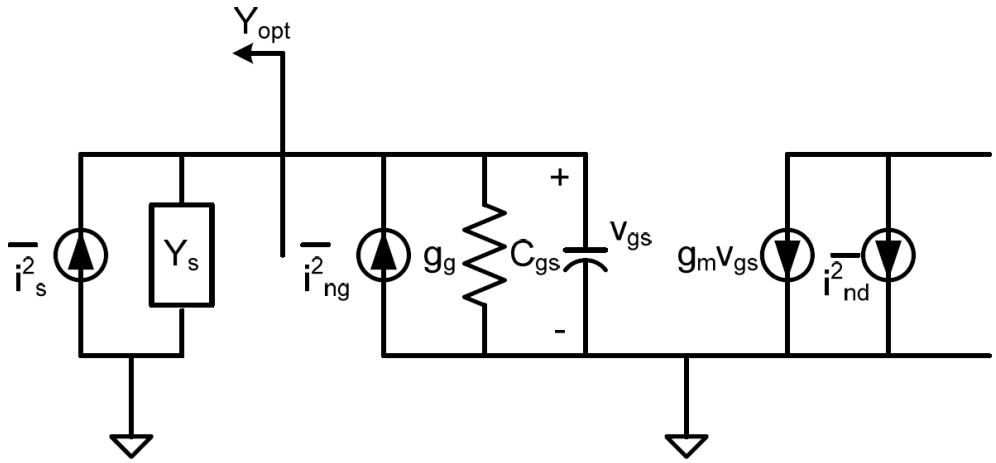

Figure 4.2. Two-port model for noise analysis in MOSFETs

$$R_n = \frac{\delta}{\alpha g_m} \tag{4.14}$$

$$G_{opt} = \alpha\omega C_{gs}\sqrt{\frac{\delta}{5\gamma}(1 - \mid c \mid^2)} \tag{4.15}$$

$$B_{opt} = -\omega C_{gs}\left(1 + \alpha \mid c \mid \sqrt{\frac{\delta}{5\gamma}}\right) \tag{4.16}$$

$$F_{min} = 1 + \frac{2}{\sqrt{5}}\frac{\omega}{\omega_r}\sqrt{\gamma\delta(1 - \mid c \mid^2)} \tag{4.17}$$

where α is the ratio of g_m and g_{d0} and its value is equal to one for long channel devices and decreases with the scaling down of the channel length.

It is indicated in the equations that as the channel length of the CMOS devices decreases, noise figure performances of these devices improve since transition frequency ω_T is inversely proportional to the effective channel length. On the other hand, g_{d0}, g_m and C_{gs} scale linearly with the device width W, while noise factors δ, γ and c are width independent. Therefore, real and imaginary parts of the optimum noise admittance are proportional to device width W while noise resistance scales inversely with W. Minimum noise factor F_{min} is independent from the device width. Since larger device width results in decrease in the noise resistance R_n, it provides the chance of lowering the noise figure and decreases the sensitivity to the deviation between termination admittance and optimum noise admittance. On the other hand, increasing the channel width for reducing noise should be considered carefully since this approach increases power consumption.

4.2.4. Linearity

Linearity is an important design consideration for an LNA in addition to noise figure, gain and input matching. Dynamic range (DR) is usually defined as the ratio of the maximum input signal level, that the circuit can tolerate, to the minimum input signal level while providing reasonable signal quality. The maximum input power that the circuit can maintain its nearly linear operation is usually defined as the upper limit of DR in low-frequency applications. However, in high-frequency applications, nonlinear effects such as intermodulation distortion or signal gain compression may limit this upper bound.

The most commonly used measures are the 1-dB compression point (P_{1dB}) and third order intercept point (IP3) [7]. When a signal of form $x(t) = A\cos\omega t$ is applied to a nonlinear system with a transfer function as in eqation 4.18, the system generates harmonics (Equation 4.19) which are frequency components that are integer multiples

of the input signal frequency.

$$y(t) = \alpha_1 x(t) + \alpha_2 x^2(t) + \alpha_3 x^3(t) \tag{4.18}$$

$$\begin{aligned} y(t) &= \alpha_1 A \cos\omega t + \alpha_2 A^2 \cos^2 \omega t + \alpha_3 A^3 \cos^3 \omega t \\ &= \alpha_1 A \cos\omega t + \frac{\alpha_2 A^2}{2}\left(1 + 2\cos 2\omega t\right) + \frac{\alpha_3 A^3}{4}\left(\cos 3\omega t + 3\cos\omega t\right) \\ &= \frac{\alpha_2 A^2}{2} + \left(\alpha_1 A + \frac{3\alpha_3 A^3}{4}\right)\cos\omega t + \frac{\alpha_2 A^2}{2} cos2\omega t + \frac{\alpha_3 A^3}{4}\cos 3\omega t \end{aligned} \tag{4.19}$$

where α_i is the ith Taylor series component.

The small signal gain of a circuit is usually obtained by ignoring harmonics. In most circuit output is a saturating or compression function of the input. As a result, when the input signal amplitude increases the gain of the circuit approaches zero for sufficiently high input levels. In RF circuits, 1-dB compression point is a measure of this effect and defined as the input signal level at which small signal gain drops 1dB below its nominal value (Figure 4.3). Since the input signals that exceed the compression point are usually clipped or saturated at the output, the dynamic range of the LNA is limited by the compression point.

The multiplication of the input signal with its harmonics is another issue that may cause signal distortion. This mixing (multiplication) produces output terms known as intermodulation products (IMP) that are not harmonics of the input frequency. In order to explain how a nonlinear system with input-output relation as in 4.18, the response to an input signal with two spectrally close frequency components (as in equation 4.20) has to be examined.

$$x\left(t\right) = a_1 \cos\omega_1 t + a_2 \cos\omega_2 t \tag{4.20}$$

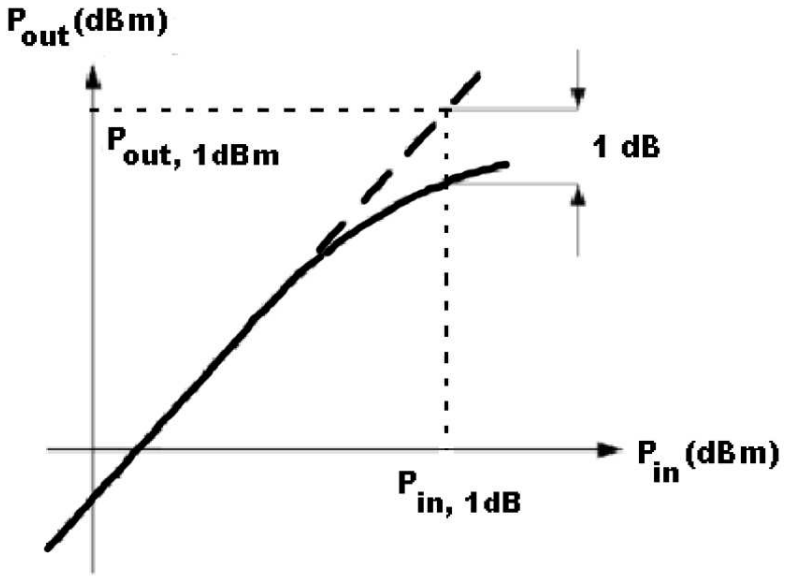

Figure 4.3. Graphical representation of 1-dB compression point

In this case, the output of the nonlinear system(given by the input output relation in equation 4.18) will be,

$$\begin{aligned} y(t) =& \alpha_1 (a_1 \cos \omega_1 t + a_2 \cos \omega_2 t) \\ &+ \alpha_2 (a_1 \cos \omega_1 t + a_2 \cos \omega_2 t)^2 \\ &+ \alpha_3 (a_1 \cos \omega_1 t + a_2 \cos \omega_2 t)^3 \end{aligned} \tag{4.21}$$

Rearranging equation 4.21, intermodulation products are obtained,

$$\omega = 2\omega_1 \pm \omega_2 : \alpha_2 A_1 A_2 \cos(\omega_1 + \omega_2)t + \alpha_2 A_1 A_2 \cos(\omega_1 - \omega_2)t \tag{4.22}$$

$$\omega = 2\omega_1 \pm \omega_2 : \frac{3\alpha_3 A_1^2 A_2}{4} \cos(2\omega_1 + \omega_2)t + \frac{3\alpha_3 A_1^2 A_2}{4} \cos(2\omega_1 - \omega_2)t \tag{4.23}$$

$$\omega = 2\omega_1 \pm \omega_2 : \frac{3\alpha_3 A_1 A_2^2}{4} \cos(2\omega_1 + \omega_2)t + \frac{3\alpha_3 A_1 A_2^2}{4} \cos(2\omega_1 - \omega_2)t \tag{4.24}$$

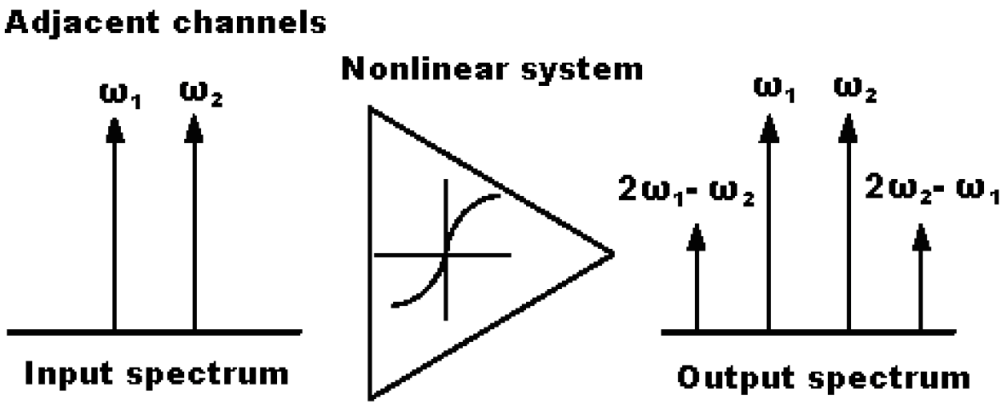

Figure 4.4. Signal spectrum of a nonlinear block

with fundamental components being,

$$\omega = \omega_1, \omega_2 : \left(\alpha_1 A_1 + \frac{3}{4}\alpha_3 A_1^3 + \frac{3}{2}\alpha_3 A_1 A_2^2\right)\cos\omega_1 t + \left(\alpha_1 A_2 + \frac{3}{4}\alpha_3 A_2^3 + \frac{3}{2}\alpha_3 A_1^2 A_2\right)\cos\omega_2 t \tag{4.25}$$

The third-order intermodulation products are at $2\omega_1 - \omega_2$ and $2\omega_2 - \omega_1$ and when ω_1 and ω_2 are close to each other, these products at $2\omega_1 - \omega_2$ and $2\omega_2 - \omega_1$ occur in the vicinity of the ω_1 and ω_2 as seen in Figure 4.4.

The third intercept point (IP3) is a performance metric which has been defined to characterize corruption of signals due to third-order intermodulation product of two close interferers and measured by two tone test in which amplitudes of the interferers are chosen to be equal. As the amplitude of the input signal increase, first-order terms do not grow as fast as the third-order intermodulation products since first-order terms increase linearly with the amplitude A while intermodulation products increase proportional to A^3 (see Figure 4.5). The input level for which fundamental terms and *IMP* at the output have the same amplitude is called third-order input intercept point

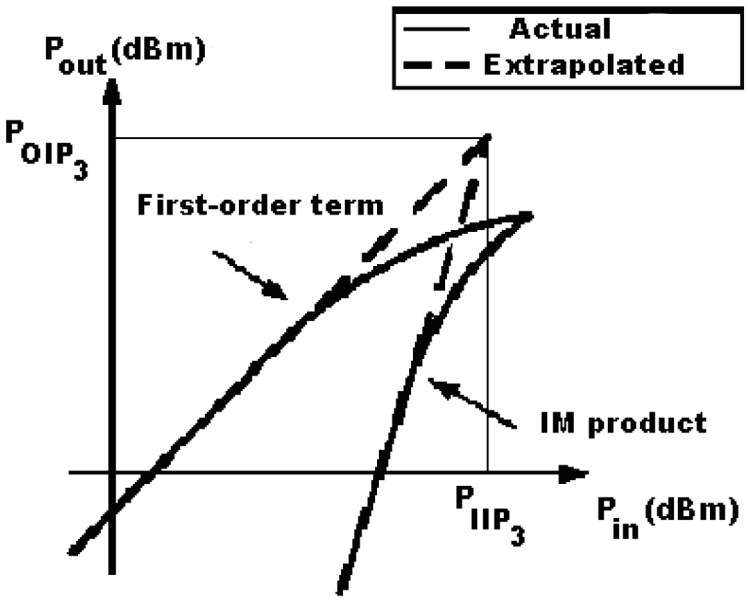

Figure 4.5. Graphical interpretation of IIP3

(IIP3) which is expressed as,

$$IIP_3 = \sqrt{\frac{4}{3}\frac{|\ \alpha_1\ |}{|\ \alpha_3\ |}} \tag{4.26}$$

4.2.5. Matching

The impedance matching concept is very important at RF circuits in order to ensure that maximum power is transferred. To ensure that maximum power is transferred both at the input and the output. Likewise to satisfy the minimum noise figure the input should also be matched to the Y_{opt} of the amplifier stage. Under these two constraints the matching has to be designed to minimize noise effects and maximize power transfer. Here a simultaneous matching strategy is required.

4.2.6. Stability

In addition to the parameters introduced in the previous sections, stability is an important concern in LNA design. LNA may become unstable for certain combinations of source and load impedances due to feedback paths from the output to the input. Stern stability factor is a constant that is used to characterize the stability of circuits and defined as [3],

$$K = \frac{1 + \Delta^2 - \mid S_{11} \mid^2 - \mid S_{22} \mid^2}{2 \mid S_{21} \mid\mid S_{12} \mid} \tag{4.27}$$

$$\Delta = S_{11}S_{22} - S_{21}S_{12} \tag{4.28}$$

When K is greater than unity and Δ is smaller than unity, then the circuit is unconditionally stable for any combination of source and load impedances. As noted in the equations, stability improves when S12 decreases due to increase in the reverse isolation of the circuit.

4.2.7. Common LNA Architectures

In the design of an LNA, there are several common goals such as minimizing the noise figure, providing gain with sufficient linearity, providing a stable input impedance and low power consumption all of which are emphasized earlier. LNA architectures can be divided into four distinct approaches, shown in Figure 4.6 [12].

In the first architecture (Figure 4.6 (a)), resistive termination is used to provide 50Ω impedance. This is the simplest method to obtain matching over a wide range of frequencies; however, the use of real resistors has destructive effects on the noise performance of the amplifier due to the thermal noise of resistive termination. Noise

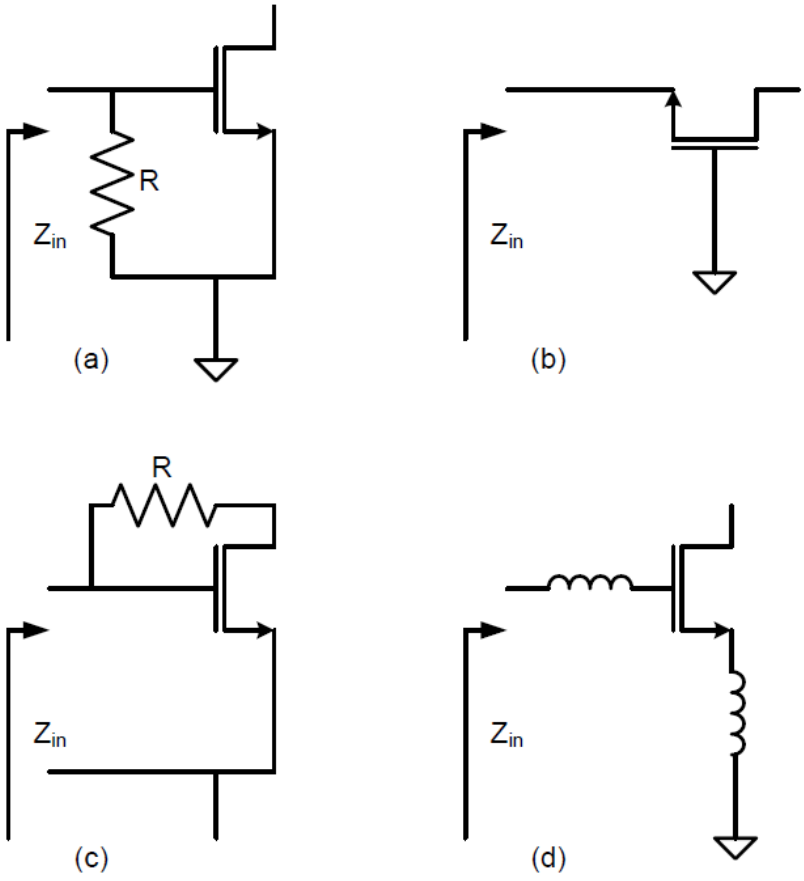

Figure 4.6. Common LNA architectures

factor of the circuit (LNA) with and without resistive termination are shown in equation 4.29 and in equation 4.30 respectively,

$$F = 2 + \frac{P_{na,i}}{kT\Delta f G_a} \tag{4.29}$$

$$F = 1 + \frac{P_{na,i}}{4kT\Delta f G_a} \tag{4.30}$$

where G_a is available power gain, $P_{na,i}$ is available noise power at the output due to the internal noise sources and Δf is the bandwidth in hertz. This degradation of performance in noise factor has two reasons; first, the added resistors own noise contribution which is equal to the noise contribution of the source resistance. Second reason is the attenuation of the input signal which causes the factor of 4 in the second term. Another downside of the resistive termination is that the input power is attenuated by the resistive divider before reaching the transistor which reduces the maximum power gain.

The second architecture (Figure 4.6 (b)) which is called $1/g_m - termination$. This architecture uses the source of a common-gate stage as the input termination. In this architecture, the impedance seen to the source terminal of the active device is $1/g_m$. With proper bias and sizing of the LNA $1/g_m = 50\Omega$ can be satisfied over a wide-band which matches the input impedance to the required impedance. It is important to mention that the gain of the first stage is constrained by the power-noise matching by the architecture. Under matching conditions, this architecture yields in the lower bound expressed in the following equation on the noise factor for CMOS amplifiers,

$$F = 1 + \frac{\gamma}{\alpha} \geqslant \frac{5}{3} \equiv 2.2dB \qquad \left(\alpha = \frac{g_m}{g_{d0}}\right) \tag{4.31}$$

where γ is the coefficient of channel thermal noise, g_m is the device transconductance,

and g_{d0} is the zero bias drain conductance. The lower bound is set for the long-channel devices, which will increase with short-channel effects and excess noise caused by hot electrons.

In figure 4.6 (c) another architecture for achieving the required matching at the input port of the LNA is using shunt feedback is presented. In this approach negative feedback provides the required impedance at the input port. This architecture also suffers from the thermal noise of the shunt resistor; however, the lower bound on noise factor is usually smaller than that of resistive and $1/g_m - termination$ architectures since it does not reduce the signal with a noisy attenuator before amplifying [7].

All three preceding architectures suffer noise figure degradation from the presence of noisy resistance in the signal path. The fourth architecture shown in Figure 4.6 (d), employs inductive source or emitter degeneration to generate a real term in the input impedance, thus this architecture overcomes the negative effects of real resistor on noise factor. Feedback techniques are often used in LNA design to shift the optimum noise impedance Z_{opt} to the desired point. Here in this architecture. series feedback has also been preferred to achieve simultaneous noise and impedance matching that is required at the input port of the LNA to deliver the maximum power from the antenna to the LNA, without degrading the noise performance of the circuit. That is why the series feedback with inductive source degeneration is applied to the common-source or cascode topologies in narrow-band applications [12].

4.3. Design and Simulation

A common-source architecture is used for the design of the LNA. A matching circuit is placed to match the impedance of the receive coil to an impedance which maximizes the input return loss and minimizes noise figure of the system. For 1.5T MRI systems the operating frequency is $63.5MHz$ and an LNA is designed and presented

in Figure 4.7. For 2.89T MRI systems the operating frequency is $123.23MHz$, the designed LNA for $64MHz$ is tweaked to operate with $123.23MHz$. The schematic of this LNA is given in Figure 4.12. The dotted region is realized in a 0.18um technology and the rest of the elements are modeled as being discrete. The die and the discrete element are connected over bonding wires which have a negligible series resistance as measured in [13]. The inductance value for the bonding wires are assumed to be $0.7nH$.

4.3.1. Design @63.5MHz

Designed LNA draws 39.6mA from a 1.8V power supply voltage. Other parameters of the LNA are given in the following figures.

As seen in Figure 4.8 a noise figure of $4.112dB$ is obtained at the operating frequency of $63.5MHz$.

In Figure 4.9 s-parameters of the designed system are plotted in rectangular format. As can be seen a sufficient gain is achieved together with low voltage reflection at both ends which indicates appropriate matching.

The designed LNA is unconditionally stable. The stability factor is presented from $5MHz$ to $60GHz$ in Figure 4.10.

Input referred third order intercept point (IIP3) simulations are performed by inserting two frequencies at $63MHz$ and $64MHz$ and harmonic balance is obtained to be $12.861dB$. The results are shown in Figure 4.11

4.3.2. Design @123MHz

Designed LNA draws 39.6mA from a 1.8V power supply voltage. Other parameters are given in the following figures.

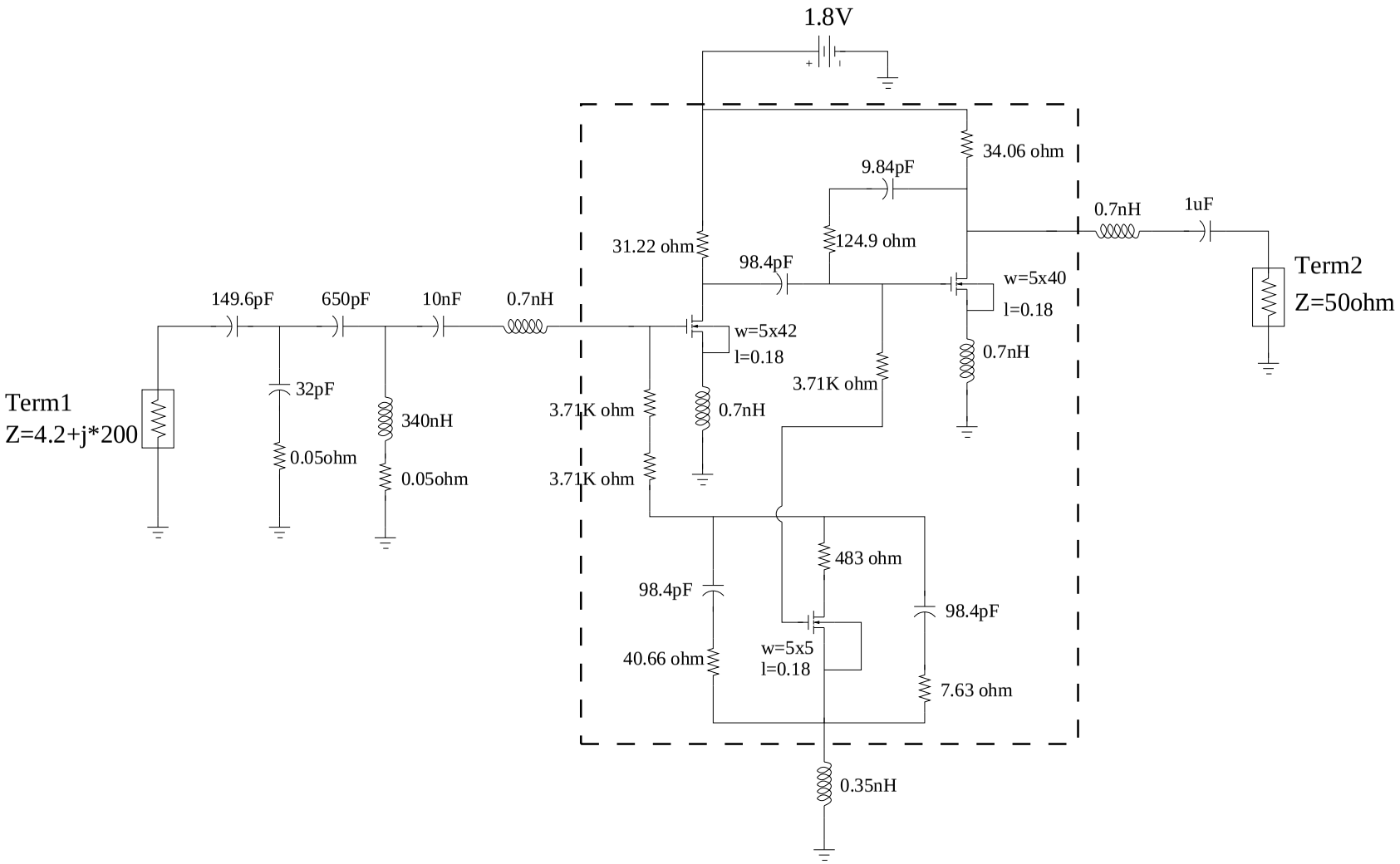

Figure 4.7. Schematic of the LNA@63.5MHz

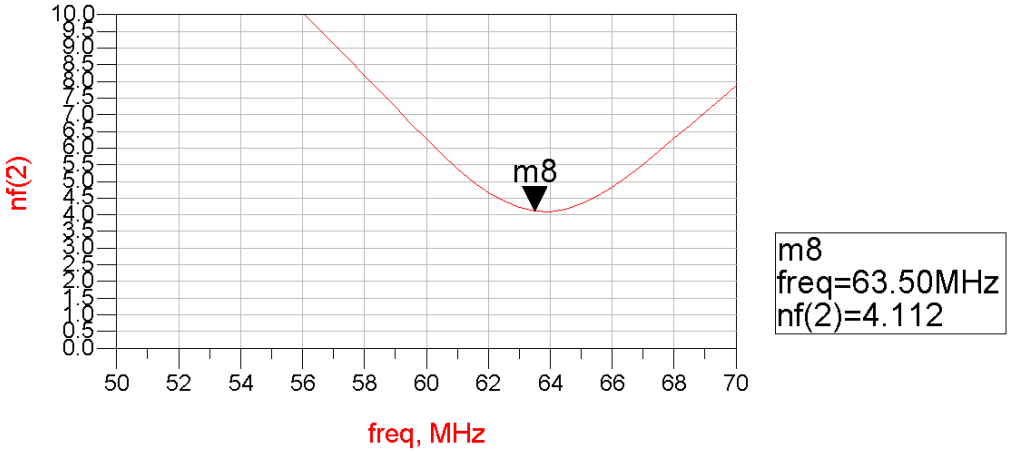

Figure 4.8. Simulated noise figure of the LNA@63.5MHz

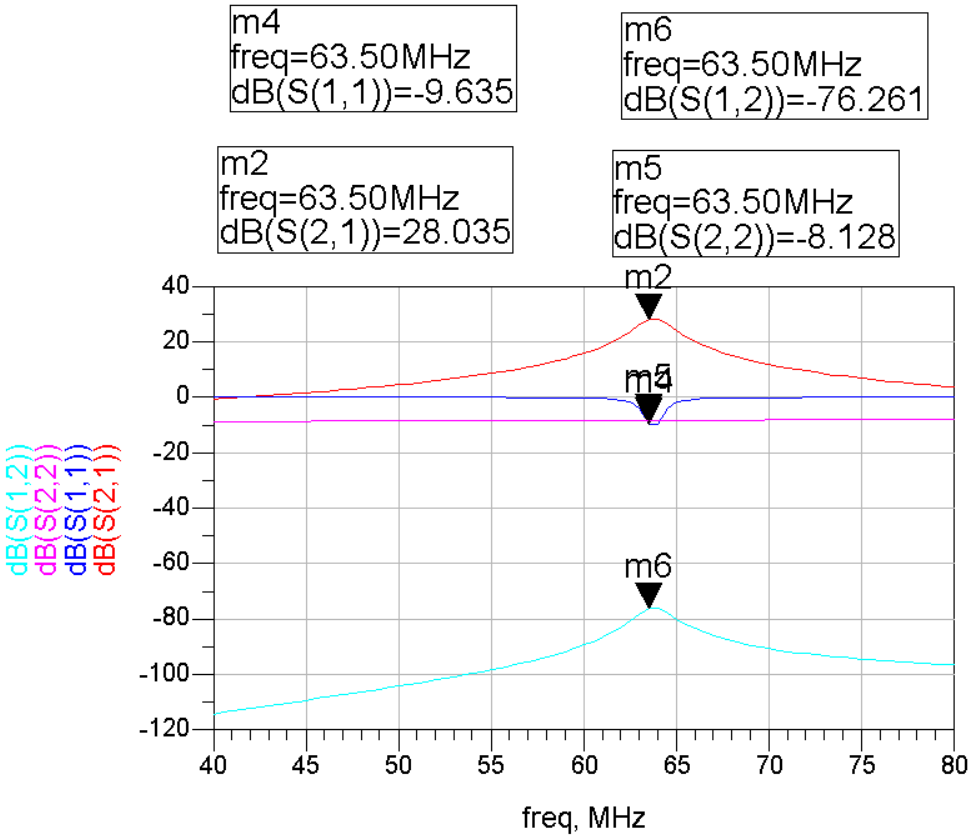

Figure 4.9. Simulated S-parameters of the LNA@63.5MHz

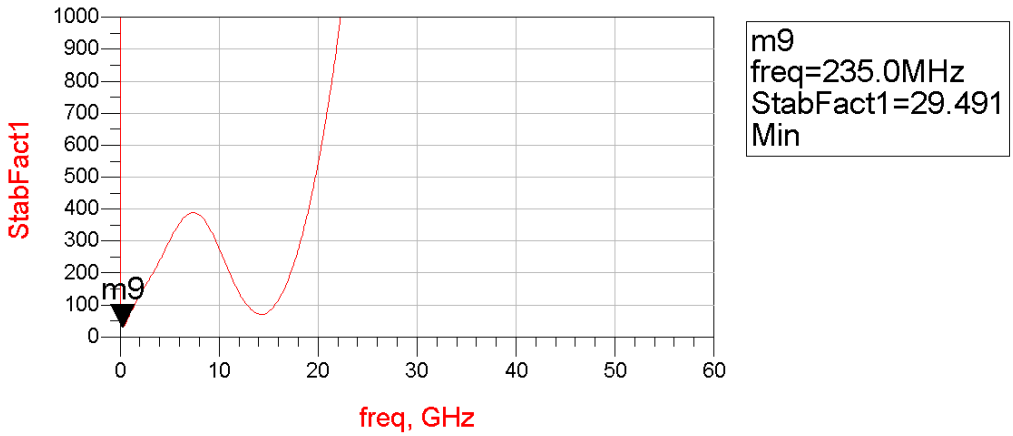

Figure 4.10. Simulated stability factor of the LNA@63.5MHz

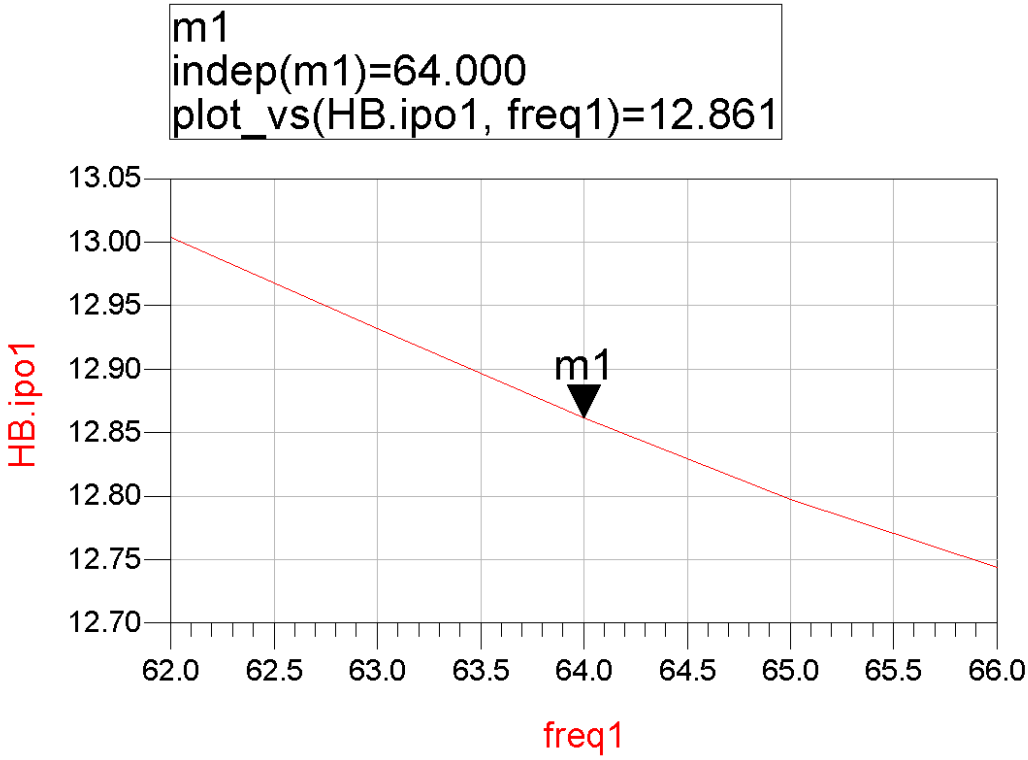

Figure 4.11. Simulated harmonic balance of the LNA@63.5MHz

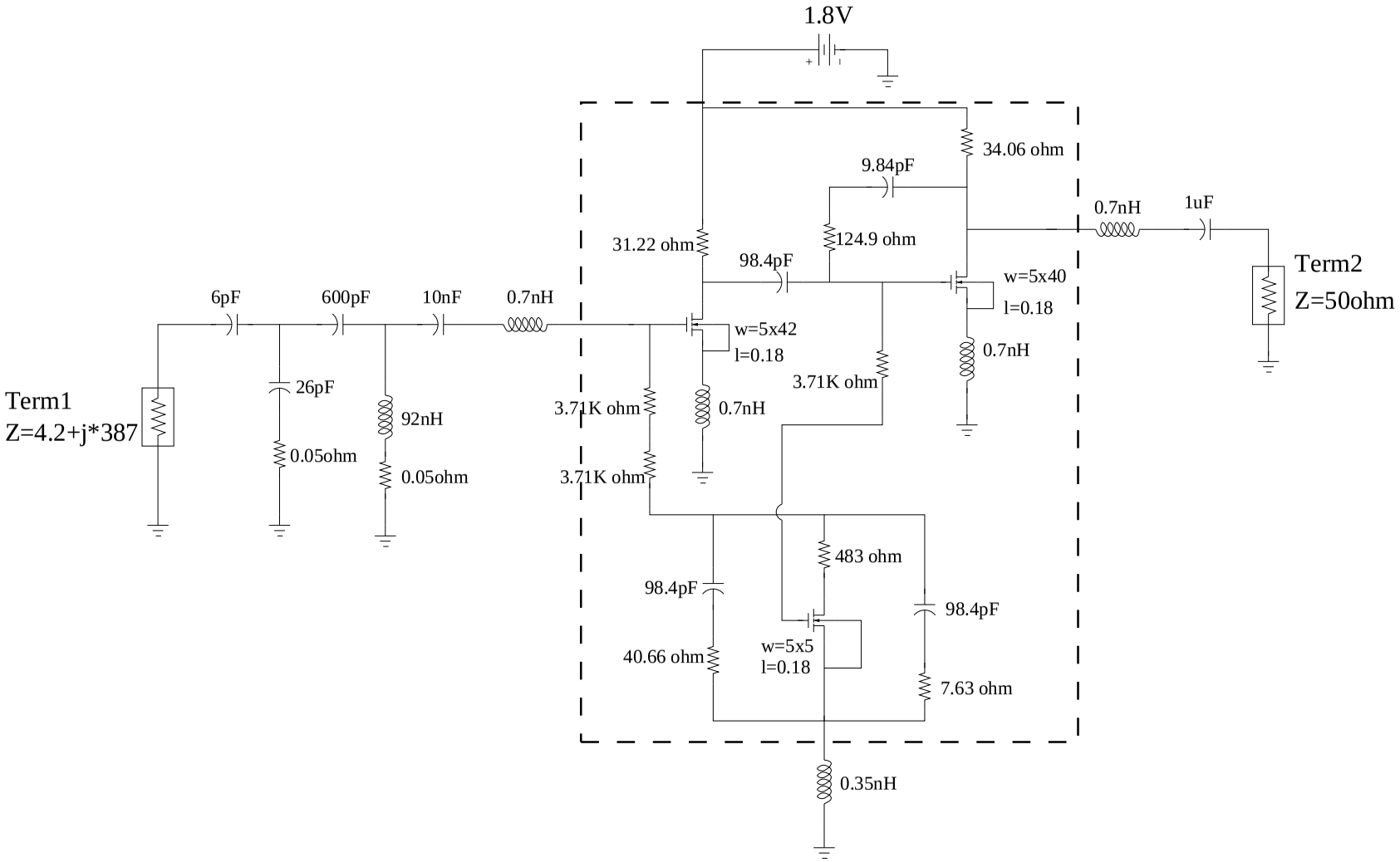

Figure 4.12. Schematic of the LNA@123MHz

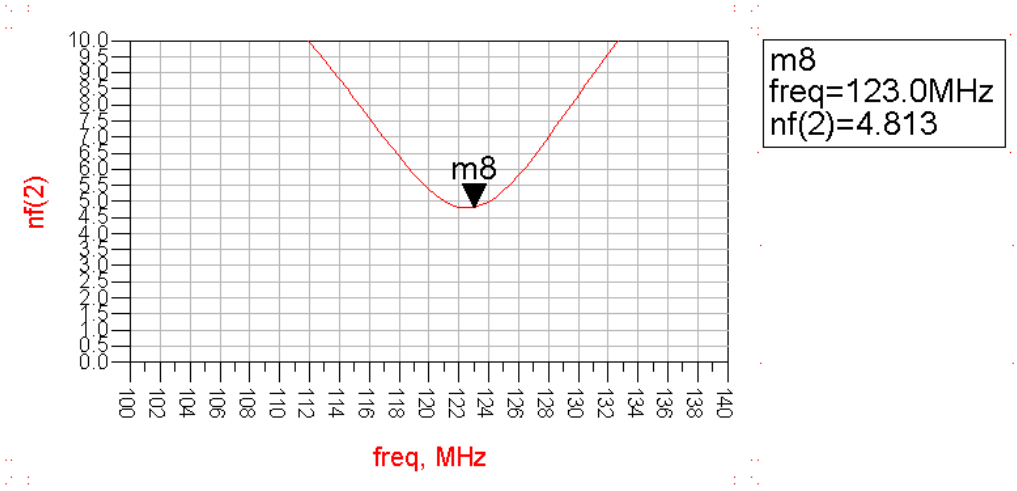

Figure 4.13. Simulated noise figure of the LNA@123MHz

As seen in Figure 4.13 a noise figure of $4.813dB$ is obtained at the operating frequency of $123MHz$.

In Figure 4.14 s-parameters of the designed system are plotted in rectangular format. As can be seen a sufficient gain is achieved together with low voltage reflection at both ends which indicates appropriate matching.

The designed LNA is unconditionally stable. The stability factor is presented from $5MHz$ to $60GHz$ in Figure 4.15.

Input referred third order intercept point (IIP3) simulations are performed by inserting two frequencies at $123MHz$ and $124MHz$ and harmonic balance is obtained to be $11.981dB$. The results are shown in Figure 4.16

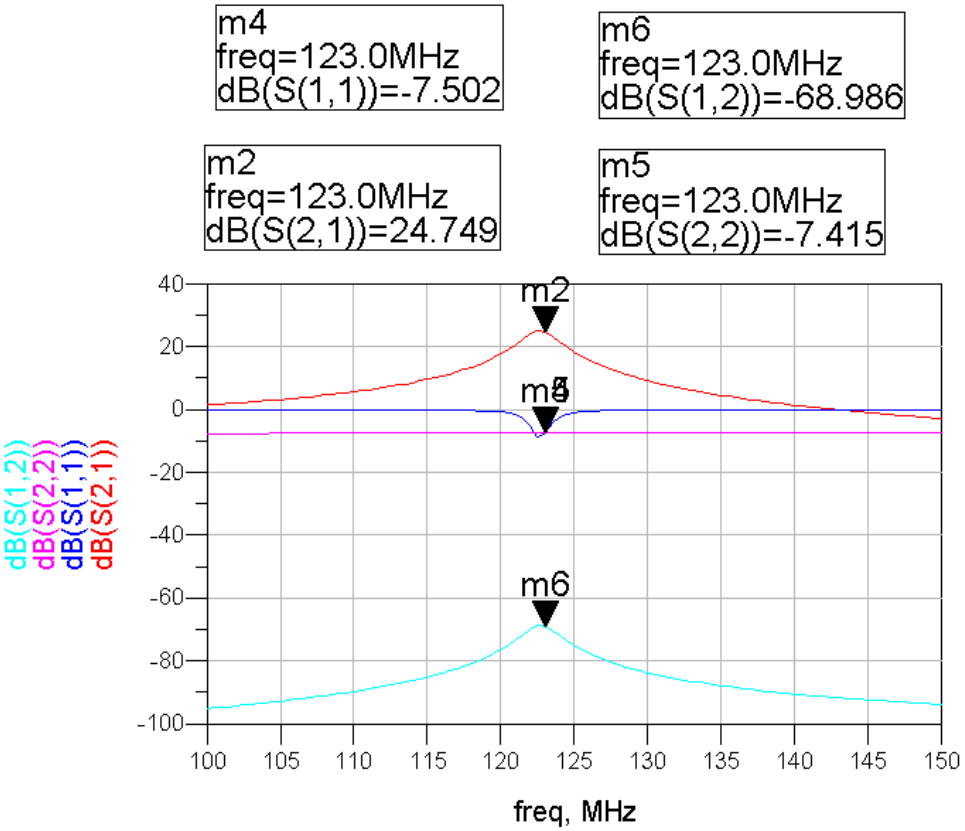

Figure 4.14. Simulated S-parameters of the LNA@123MHz

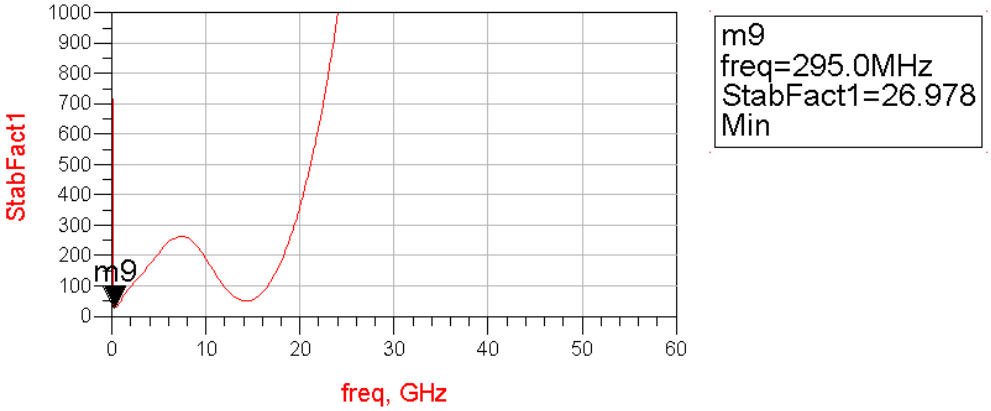

Figure 4.15. Simulated stability factor of the LNA@123MHz

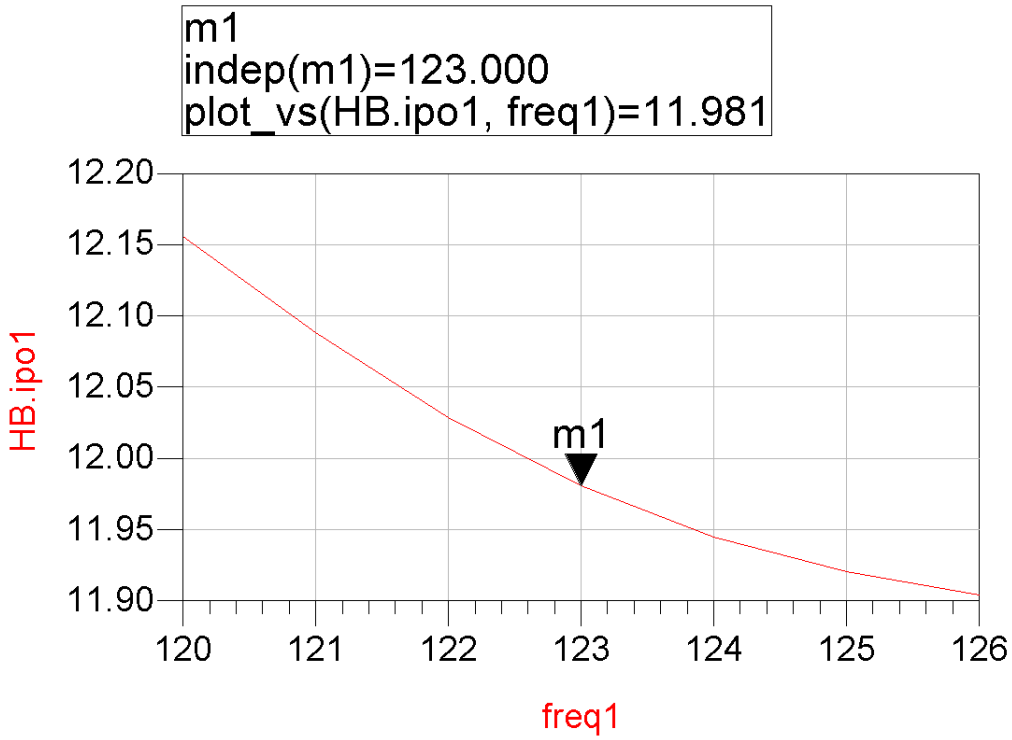

Figure 4.16. Simulated harmonic balance of the LNA@123MHz

5. Conclusion and Future Work

In this study front-end building blocks were designed for an active localization system. Analog design of a charge pump stage and a low noise amplifier has been done with constraints present in MRI systems.

A planar receive antenna for receiving MRI signals is studied. Antennas with different sizes were drawn under constraints of the production process. A 3-D wave solver is used to generate electrical model from the geometrical representation for the studied coils. The coils were produced and matched to 50Ω impedance to be used in further measurements in MR systems. In addition larger coils with higher turn counts are simulated to be used in resonant matched input stage.

The designed dickson charge pump operates with an alternating input signal at 100MHz with an amplitude of 1V and generates 1.94V at its output for 100K ohm load resistance. For the receive coils results show that Q^2xR values of 1300 can be reached with the processing technology at hand for the resonant matching approach. Resonant matching architecture for the receive front-end can be studied further to get better noise figure results. The gain stage is designed as a Low Noise Amplifier, for 64MHz and 123MHz precession frequencies. $4.112dB$ noise figure is obtained for LNA@64MHz and $4.813dB$ for LNA@123MHz respectively. Both designed LNAs draw 39.6mA current from the power supply.

The study can be extended by the resonant matched input stage which present lower noise figure values. The technology to produce receive antenna can be revisited to support coils with higher quality factors in a smaller area. Micro-machined coils promise for higher quality factor values hence better Q^2xR values.

REFERENCES

1. Nyenhuis, J., S. Park, R. Kamondetdacha, A. Amjad, F. Shellock, and A. Rezai, "MRI and implanted medical devices: basic interactions with an emphasis on heating," *IEEE Transactions on Device and Materials Reliability*, vol. 5, no. 3, pp. 467–480, 2005.

2. Yeung, C., R. Susil, and E. Atalar, "RF safety of wires in interventional MRI: using a safety index," in *Engineering in Medicine and Biology Society, 2001. Proceedings of the 23rd Annual International Conference of the IEEE*, vol. 3, 2001.

3. Yuan, J., J. Wei, and G. Shen, "A 4-Channel Coil Array Interconnection by Analog Direct Modulation Optical Link for 1.5-T MRI," *IEEE Transactions on Medical Imaging*, vol. 27, no. 10, pp. 1432–1438, 2008.

4. Memis, O., Y. Eryaman, O. Aytur, and E. Atalar, "Miniaturized fiber-optic transmission system for MRI signals," *Magnetic Resonance in Medicine*, vol. 59, no. 1, pp. 165–173, 2008.

5. Fandrey, S., S. Weiss, and J. Muller, "Development of an active intravascular MR device with an optical transmission system," *IEEE Transactions on Medical Imaging*, vol. 27, no. 12, pp. 1723–1727, 2008.

6. Sun, N., Y. Liu, H. Lee, R. Weissleder, and D. Ham, "CMOS RF Biosensor Utilizing Nuclear Magnetic Resonance," *IEEE Journal of Solid-State Circuits*, vol. 44, no. 5, pp. 1629–1643, 2009.

7. Lee, T., *The design of CMOS radio-frequency integrated circuits*. Cambridge University Press, 2004.

8. Razavi, B., *RF microelectronics*. Prentice-Hall, Inc. Upper Saddle River, NJ, USA, 1998.

9. Van der Ziel, A., "Noise in solid-state devices and lasers," *Proceedings of the IEEE*, vol. 58, no. 8, pp. 1178–1206, 1970.

10. Jindal, R., "Noise associated with distributed resistance of MOSFET gate structures in integrated circuits," *IEEE Transactions on Electron Devices*, vol. 31, no. 10, pp. 1505–1509, 1984.

11. Goo, J., H. Ahn, D. Ladwig, Z. Yu, T. Lee, R. Dutton, A. Inc, and C. Sunnyvale, "A noise optimization technique for integrated low-noise amplifiers," *IEEE Journal of Solid-State Circuits*, vol. 37, no. 8, pp. 994–1002, 2002.

12. Shaeffer, D. and T. Lee, "A 1.5-V, 1.5-GHz CMOS low noise amplifier," *IEEE Journal of Solid-State Circuits*, vol. 32, no. 5, pp. 745–759, 1997.

13. Qi, X., P. Yue, T. Arnborg, H. Soh, H. Sakai, Z. Yu, and R. Dutton, "A fast 3 D modeling approach to electrical parameters extraction of bonding wires for RF circuits," *IEEE Transactions on Advanced Packaging*, vol. 23, no. 3, pp. 480–488, 2000.